

# Two-dimensional DEM-FEM coupling analysis of seismic failure and anti-seismic measures for concrete faced rockfill dam

Yongqian Qu<sup>a,b</sup>, Degao Zou<sup>a,b,\*</sup>, Jingmao Liu<sup>a,b</sup>, Zhikai Yang<sup>a,b</sup>, Kai Chen<sup>a,b</sup>

<sup>a</sup> State Key Laboratory of Coastal and Offshore Engineering, Dalian University of Technology, Dalian 116024, China

<sup>b</sup> School of Hydraulic Engineering, Dalian University of Technology, Dalian 116024, China

## ARTICLE INFO

### Keywords:

Concrete faced rockfill dam  
Polygonal DEM  
DEM-FEM coupling analysis  
Seismic failure  
Anti-seismic measures

## ABSTRACT

The concrete faced rockfill dam is composed of granular materials and the failure pathways typically exhibits multi-scale mechanical behavior. In this paper, a 2D polygonal DEM-FEM interface coupling analysis program is developed and introduced to the failure analysis of a 100 m high CFRD under strong earthquake. The polygonal DEM is developed to describe the strong-nonlinearity, large deformation and discontinuous of dam. The FEM and seismic wave input method is combined to simulate the dam-foundation interaction. A bonded model is proposed to describe the deformation characteristics of face slab and anti-seismic measure. The results indicate that the initial seismic failure of CFRD occurs at the crest zone, and is characterized by the loosening, sliding and even rolling away of the shallow rockfill on the slope. Other initial failure modes include settlement of the dam crest, separation between the face slab and rockfill, downstream sliding of the wave wall and separation between wave wall and face slab. The installation of a nailed protective slab at the upper part of the downstream slope reduces the seismic damage by 27–41 %. The analysis method can intuitively reproduce the seismic failure mode and failure evolution of the CFRD and quantify the effect of the anti-seismic measure.

## 1. Introduction

Concrete faced rockfill dams (CFRDs) have become a more popularly implemented dam type due to reliability, cost effectiveness and the adaptability to various environments and climates (Kartal et al., 2010; Kim and Kim, 2008; Zarfl et al., 2015). Many high CFRDs are constructed in meizoseismal areas, such as the Jinglintai dam (height of 157 m), the Zipingpu dam (height of 156 m), and the Gongboxia dam (height of 132 m) (Qu et al., 2019). There are some CFRDs are damaged by the earthquake, such as Cogoti CFRD in Chile, Minase CFRD in Japan, Malpasse CFRD in Peru, Cogswell CFRD in America, and Zipingpu CFRD in China (Boulanger et al., 1995; Kong et al., 2016; Luis et al., 1985; Zhang et al., 2015; Zou et al., 2013). Under strong earthquake, the dam is contracted and sank, shallow rockfill in the slope is loosening, slipping and even rolling, the face slab is crushed and separated from rockfill, the vertical joints and peripheral joint are open and slipping. These disasters have seriously affected the normal operation of the dam. The seismic safety of these dams has received widespread concern and attention. And it is necessary to study the seismic failure characteristics and anti-seismic measures of CFRDs.

Dam materials are treated as discrete particles in the micro-scale;

however, at the macro-scale, dam materials are usually treated as a continuum. Based on the finite element method (FEM) and other continuum mechanics methods, researchers have put forward many constitutive models to reflect the nonlinear, elastic-plastic, dilatancy and anisotropy of macroscopic mechanical properties (Liu et al., 2014a, 2014b, 2018; Ning et al., 2020; Saberi et al., 2019; Xiao et al., 2016), all of which have been widely used in practical engineering problems (Chen et al., 2018a; Kong et al., 2016; Liu et al., 2020; Qu et al., 2021; Yu et al., 2021, 2022; Zou et al., 2013). These methods can help analyze the macroscopic seismic response characteristics of concrete faced rockfill dams (CFRDs), and are commonly used for dynamic analysis of CFRDs under medium and low earthquakes. However, in the case of strong earthquakes, large deformations and severe, discontinuous local damage (e.g. looseness, slipping and rolling of rockfill materials) can occur in the CFRD. It is difficult for the traditional, continuum mechanics based FEM to accurately and efficiently reproduce such failure process.

The CFRD is a multi-scale structure composed of granular materials. The dynamic failure of the dam is therefore also multi-scale, with mechanical events occurring from the microscopic particle scale to the macroscopic site scale. The discrete element method (DEM), which based on discontinuous mechanics, is well known as an effective method

\* Corresponding author at: State Key Laboratory of Coastal and Offshore Engineering, Dalian University of Technology, Dalian 116024, China.

E-mail address: [zoudegao@dlut.edu.cn](mailto:zoudegao@dlut.edu.cn) (D. Zou).

<https://doi.org/10.1016/j.compgeo.2022.104950>

Received 8 February 2022; Received in revised form 30 July 2022; Accepted 31 July 2022

Available online 9 August 2022

0266-352X/© 2022 Elsevier Ltd. All rights reserved.

to study the mechanical behavior of granular materials at the micro-scale and has been widely used in geotechnical engineering (Zhao et al., 2018; Liu, 2021). However, in CFRD research, the DEM is so far primarily used to study the material properties of rockfill materials (Kh et al., 2011; Ma et al., 2019; Zhou et al., 2018, 2020;), and there are few studies related to the use of DEM for structural analysis and engineering. Deluzarche and Cambou (2006) carried out a two-dimensional static analysis of a 20 m-high CFRD to investigate the influence of particle breakage on dam deformation while the dam is being constructed. Silvani et al. (2008) studied the causes of rockfill settlement during initial water storage. Their study considered the influence of buoyancy force and friction between particles but did not analyze the whole dam. Liu and Yang (2009) simulated the shaking table test of an earth-rock dam using a two-dimensional particle flow method and analyzed the influence of particle bond strength and seismic peak acceleration on the dynamic characteristics of the dam. Tran et al. (2009) carried out static analysis of a 20 m high two-dimensional dam, and analyzed the influence of rock aging on the dam during service operation. Liu et al. (2010) discretized a two-dimensional 10 m high rockfill dam into 9000 circular particles and studied the particle breakage characteristics of the dam during filling and impoundment using two-dimensional Particle Flow Code (PFC2D).

At present, there is limited research and application of DEM in earth-rock dam engineering. Meanwhile, there are some limitations of the research. First, circular particles cannot accurately describe the influence of the particle shape. Secondly, the limited number of particles leads to gradation distortion. Thirdly, the dam height in simulation does not exceed 20 m, which cannot reflect the characteristics of higher dams. Finally, the research is mainly concentrated in the construction period, with minimal focus on seismic damage.

A principal obstacle to adoption of DEM for seismic analysis is the computational efficiency. DEM is inefficient in dealing with large scale boundary value problems. Even though computing power is developing rapidly, it is impossible to discretize the entire macro domain of the CFRD as particle aggregation for numerical simulation.

Multi-scale methods can take full advantage of continuum mechanics and discrete element method, and can alleviate or even avoid their shortcomings. FEM-DEM coupling is a multi-scale method commonly used in geotechnical engineering, such as for slopes, underground structures, retaining walls and pile foundations (Powrie et al., 2002; Saia, 2010; Song et al., 2019; Tu et al., 2017; Zhao et al., 2018). However, there has been limited research in the application of DEM-FEM towards CFRD mainly because of the large scale of engineering, complexity in geological structure, multiple influencing factors and heavy computational burden. At present, a large portion of the coupling analysis often requires multiple software (such as PFC-FLAC), resulting in large functional limitations and low efficiency, which is difficult to overcome in complex static and dynamic analysis requirements of CFRD. Therefore, the development of efficient DEM-FEM coupling analysis method and software, and the multi-scale analysis of the seismic response of CFRDs will be helpful towards better understanding their seismic failure mode and how damage evolves in the dam.

In this paper, an independent, two-dimensional polygonal DEM analysis program under the same solving framework is first developed, and integrated to the FEM software GEODYNA (Zou and Kong, 2003), and then the DEM-FEM interface coupling failure analysis of a CFRD considering dam-foundation interaction under strong earthquake is carried out. A bonded model is proposed to describe the deformation characters of face slab and anti-seismic measure. The failure mode of dam crest zone and the effect of anti-seismic measures is studied and quantified. The research provides theoretical and technical support for safety evaluation and seismic design of high CFRDs.

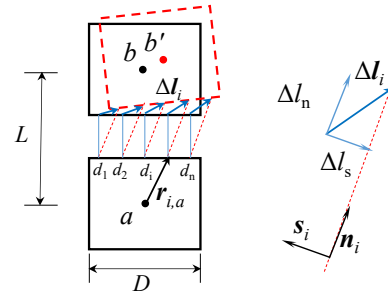


Fig. 1. The bond model.

## 2. Theory introduction

### 2.1. Discrete element method

The discrete element method was proposed by Cundall and Strack (1979) to study rock slopes with joint fissures. The method is based on discontinuous medium mechanics, which can describe the structure and motion of granular material. In DEM analysis, the computational domain is firstly divided into a series of discrete rigid particles, which can be translated, rotated and separated from each other. In the calculation, the contact force is firstly calculated according to the embedding quantity between the particles, and then the motion state of the particles is updated. The explicit method is used to solve the equations of motion. The main formulas are shown in the appendix A and the detailed introduction to DEM can be found in literature (Luding, 2006) and references therein.

In this paper, the normal penetration procedure is used for the calculation of normal force, which may lead to non-conservative results if penetration comes in one side and exits from another. In the simulation, the overlap is very small and the penetration can be avoided by adjusting the contact stiffness and time step. Generally, when particles penetrate each other, there will be a large contact force (acceleration) that causes the system to gradually diverge from there. The parameters can be adjusted in time by monitoring certain physical indexes (such as the energy of the system, maximum acceleration, maximum overlap/radius) to avoid the penetration.

### 2.2. a developed continuum deformation simulation method

The discrete element particles are rigid bodies, which cannot describe the deformation characteristics of continuous bodies like face slabs, cut-off walls, wave walls and slope protection structures. These deformation characteristics can significantly affect the dam response. For example, the separation between the face slab and rockfill will be overestimated by not considering the deformation of the concrete face slab. Also, the effect of reinforcement will be overestimated by not considering the deformation of slope protection structure. Therefore, this paper proposes a bond model between polygonal particles to describe the continuum deformation.

As shown in Fig. 1, a series of springs are set between the two opposing edges of particles a and b. The length of the edge on each particle is D and the distance between the particle barycentre is L. When the two particles move, the normal and tangential displacements of spring i are.

$$\Delta l_{i,n} = \Delta \mathbf{l}_i \cdot \mathbf{n}_i \quad (1)$$

$$\Delta l_{i,s} = \Delta \mathbf{l}_i \cdot \mathbf{s}_i \quad (2)$$

where  $\Delta \mathbf{l}_i$  is the relative displacement of the two nodes of the spring i,  $\Delta l_{i,x}$  and  $\Delta l_{i,y}$  are the normal and tangential relative displacement components of the nodes of spring i, respectively. The relative velocity  $\Delta \mathbf{v}_i$  of the two nodes of the spring i is.

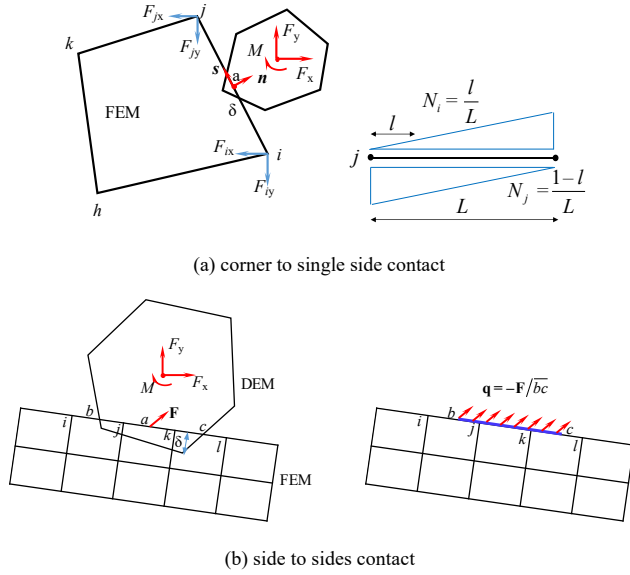


Fig. 2. The interface coupling between FEM and DEM.

$$\Delta \mathbf{v}_i = \mathbf{v}_a - \mathbf{v}_b + \boldsymbol{\omega}_a \times \mathbf{r}_{a,i} + \boldsymbol{\omega}_b \times \mathbf{r}_{b,i} \quad (3)$$

$$\Delta \mathbf{v}_{i,n} = \Delta \mathbf{v}_i \cdot \mathbf{n}_i, \Delta \mathbf{v}_{i,s} = \Delta \mathbf{v}_i \cdot \mathbf{s}_i \quad (4)$$

where  $\mathbf{v}_a$  and  $\mathbf{v}_b$  are the translational velocities of the barycentre of particles  $a$  and  $b$ , respectively,  $\boldsymbol{\omega}_a$  and  $\boldsymbol{\omega}_b$  are the rotational velocities of particles  $a$  and  $b$  relative to the spring nodes, respectively,  $\Delta \mathbf{r}_{i,a}$  and  $\Delta \mathbf{r}_{i,b}$  are the radius vectors from the barycentre of particles  $a$  and  $b$  to the spring nodes, respectively, and  $\Delta \mathbf{v}_{i,n}$  and  $\Delta \mathbf{v}_{i,s}$  are the normal and tangential components of the relative velocities of the two nodes in spring  $i$ , respectively. The internal force of spring  $i$  is.

$$F_{i,n} = k_n \Delta l_{i,n} / L - \gamma_n \Delta v_{i,n} \quad (5)$$

$$F_{i,s} = k_s \Delta l_{i,s} / L - \gamma_s \Delta v_{i,s} \quad (6)$$

where  $F_{i,n}$  and  $F_{i,s}$  are the normal and tangential stresses of spring  $i$ ,  $k_n$  and  $k_s$  are the normal and tangential stiffness of spring  $i$ , and  $\gamma_n$  and  $\gamma_s$  are the normal and tangential damping coefficients of spring  $i$ , respectively. The force and moment of particle  $a$  is.

$$\mathbf{F}_a = \sum_i d_i (F_{i,n} \mathbf{n}_i + F_{i,s} \mathbf{s}_i) \quad (7)$$

$$\mathbf{M}_a = \sum_{i=1}^n d_i \|\mathbf{r}_{i,a}\| (F_{i,n} \mathbf{n}_i + F_{i,s} \mathbf{s}_i) \cdot \mathbf{t}_{i,a} \quad (8)$$

where  $\mathbf{F}_a$  and  $\mathbf{M}_a$  are respectively the force and moment of particles  $a$ ,  $d_i$  is the characteristic width of spring  $i$ ,  $D = \sum_{i=1}^n d_i$ , and  $\mathbf{t}_{i,a}$  is the unit vector of  $\mathbf{r}_{i,a}$  after rotating 90 degrees counter-clockwise. The force on particle  $b$  is equal to  $\mathbf{F}_a$ , but it acts in the opposite direction, and the moment is.

$$\mathbf{M}_b = \sum_{i=1}^n d_i \|\mathbf{r}_{i,b}\| (-F_{i,n} \mathbf{n}_i - F_{i,s} \mathbf{s}_i) \cdot \mathbf{t}_{i,b} \quad (9)$$

### 2.3. DEM-FEM interface coupling method

In the interface coupling analysis using DEM and FEM, force boundary conditions are adopted. Elements from conventional FEM serves as a wall against DEM-based elements, and are in contact with the particles. The contact force is computed by the particle-wall contact type in the DEM analysis, and is then applied to both the DEM-based particles and FEM-based elements.

For a quadrilateral element, the shape function of the sides is linear, as shown in Fig. 2, where.

$$N_i = \frac{l}{L}, N_j = 1 - \frac{l}{L} \quad (10)$$

and  $L = |\mathbf{x}_i - \mathbf{x}_j|$  is the edge length of the element,  $l$  is the distance from a point on the edge of the finite element element to the node. The midpoint of the contact line is Point A and the overlap is  $\delta$ . The normal and shear directions  $\mathbf{n}$  and  $\mathbf{s}$  are.

$$\mathbf{s} = \frac{\mathbf{x}_j - \mathbf{x}_i}{|\mathbf{x}_j - \mathbf{x}_i|}, \mathbf{n} = (s_y, -s_x) \quad (11)$$

The velocity at Point A is.

$$\mathbf{v}_a = N_i \mathbf{v}_i + N_j \mathbf{v}_j \quad (12)$$

Thus, the normal and tangential contact forces  $\mathbf{n}F_n$  and  $\mathbf{s}F_s$  can be obtained according to the particle-wall contact mode in DEM. In the FEM domain, the contact forces need to be converted into nodal force,

$$\mathbf{F}_i = -N_i (\mathbf{n}F_n + \mathbf{s}F_s), \mathbf{F}_j = -N_j (\mathbf{n}F_n + \mathbf{s}F_s) \quad (13)$$

where  $\mathbf{F}_i$  and  $\mathbf{F}_j$  are the contact forces on nodes  $i$  and  $j$  of the FEM element.

The side to side contact between FEM-FEM is shown as Fig. 2(b), which involves more than one finite elements. Comparing with DEM corner to a single side of the FEM interaction as shown in Fig. 2(a), the difference lays in the conversion from contact forces into nodal force for FEM analysis. Uniform pressure  $\mathbf{q}$  can be obtained through the contact force and contact length, as shown in Fig. 2(b). Then, the nodal force can be calculated as follow.

$$\mathbf{F}_i = N_i \bar{b} \bar{j} \mathbf{q}, N_i = \frac{0.5 \bar{b} \bar{j}}{\bar{i} \bar{j}} \quad (14)$$

$$\mathbf{F}_j = N_j \bar{b} \bar{j} \mathbf{q} + 0.5 \bar{j} \bar{k} \mathbf{q}, N_j = \frac{1 - 0.5 \bar{b} \bar{j}}{\bar{i} \bar{j}} \quad (15)$$

$$\mathbf{F}_k = 0.5 \bar{j} \bar{k} \mathbf{q} + N_k \bar{k} \bar{c} \mathbf{q}, N_k = \frac{1 - 0.5 \bar{k} \bar{c}}{\bar{k} \bar{l}} \quad (16)$$

$$\mathbf{F}_l = N_l \bar{k} \bar{c} \mathbf{q}, N_l = \frac{0.5 \bar{k} \bar{c}}{\bar{k} \bar{l}} \quad (17)$$

This is a simple way to distribute the contact force in DEM-FEM coupling method, which may violate the rotational equilibrium if the centroid penetrate particles or elements. However, as the statement at Section 2.1, the particle-particle and particle-finite element overlap can be made very small by adjusting the contact stiffness and time step. Generally, the centroid will not penetrate particles or elements, so the correctness of the contact force distribution can be guaranteed. Due to

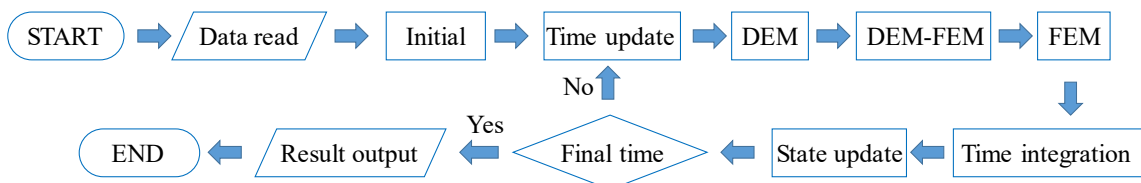


Fig. 3. Flowchart for performing coupled analysis.

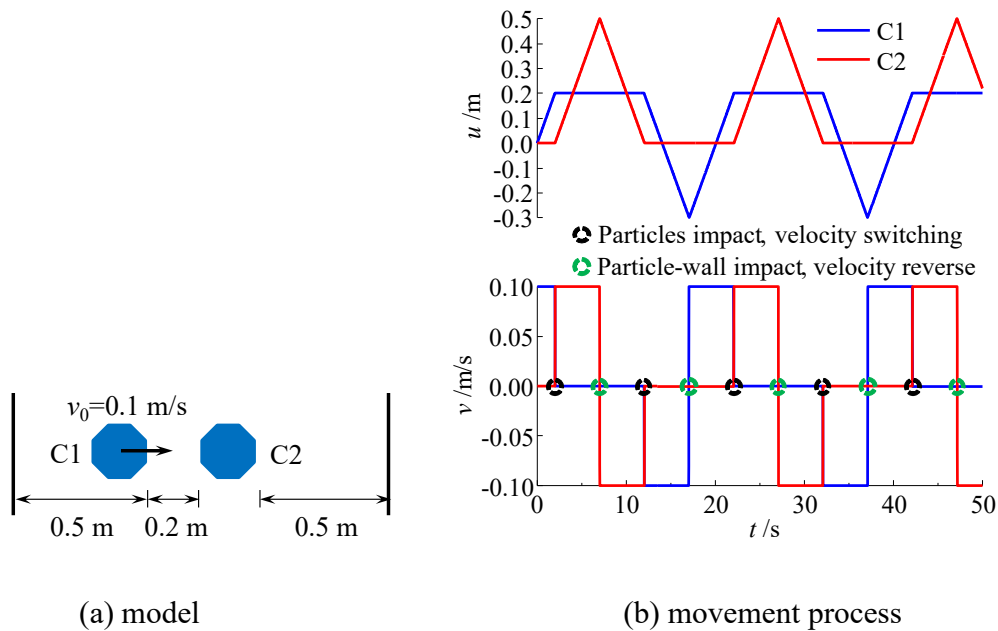


Fig. 4. Simple impact of two particles.

the large scale of the CFRD project and the heavy computational burden, the simple method is adopted to improve computational efficiency.

The DEM are integrated to the FEM software GEODYNA (Zou and Kong, 2003), which has been widely used to the static and dynamic analysis of rockfill dam (Chen et al., 2018a; Kong et al., 2016; Qu et al., 2019,2021; Yu et al., 2021, 2022; Zou et al., 2013). The process for performing coupling analysis is shown in Fig. 3. The information from the FEM domain is firstly transmitted to DEM as boundary conditions; meanwhile, initialization operations such as space application are carried out. During each time step, the motion state of coupling boundary is updated, then the DEM domain is analysed and the nodal force at the coupling boundary is obtained and returned to the FEM domain. The nodal force is superimposed on the external load vector, and then the FEM domain is solved. This program adopts an object-oriented design method for DEM-FEM coupling and can achieve flexible multi-region coupling analysis by setting up an appropriate number of class objects.

#### 2.4. Non-uniform seismic wave input method

The energy of dam-valley-foundation system is open (Xu et al., 2018). The external scattered energy will radiate to the infinite foundation, resulting in the difference in the dynamic response at each point of the dam boundary. The interactions between the valley, foundation and dam should be considered. In addition, with the increase in dam height, the effect of seismic wave characteristics on the seismic response of the CFRD can be significant. The results from Kong et al.,(2019) indicated that the traditional vibration analysis method overestimated the dynamic response of high rockfill dam 10 %-50 %. Therefore, the non-uniform seismic wave input method is necessary to investigate the seismic response of the CFRD. The non-uniform seismic wave input method is realized using a viscous-spring artificial boundary and equivalent nodal loads (Liu et al., 2006).

### 3. Method and Procedure Verification

#### 3.1. Single particle example

Fig. 4(a) illustrates two identical particles C1 and C2 that are 0.2 m apart. The particle C1 moves toward particle C2 at a velocity of 0.1 m/s, and the gravity and damping are not considered in the analysis. Fig. 4(b)

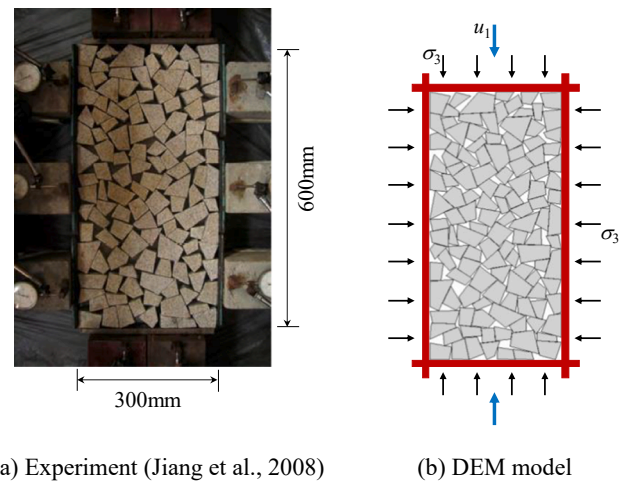


Fig. 5. The biaxial test of coarse-grained soil.

is the displacement and velocity history of the two particles. At 2.0 s, the particles collide and exchange velocity. Particle C2 moves to the right at the velocity of 0.1 m/s, and makes contact with the wall at 7.0 s whereupon the direction of the velocity is reversed. The results are consistent with the theoretical analysis.

#### 3.2. Biaxial compression test of coarse aggregate

Jiang et al. (2008) conducted a two-dimensional compression test on granular soil. The material is granite, and cut into irregular polygonal prisms with a height of 40 mm. The cross-section shapes are mostly 4-sided, with a small number of triangles and pentagons. Granular soils are modelled as aggregates of these polygonal prismatic particles, as shown in Fig. 5(a), and have a sample size of 300 ~ 600 mm. During the test, the vertical and lateral compressions were carried out with a certain pressure before keeping the lateral pressure constant. The vertical pressure was slowly applied until the sample was destroyed. The test conducted three confining pressures of 200 kPa, 400 kPa and 600 kPa. The polygon DEM model is shown in Fig. 5(b). In the model, the normal



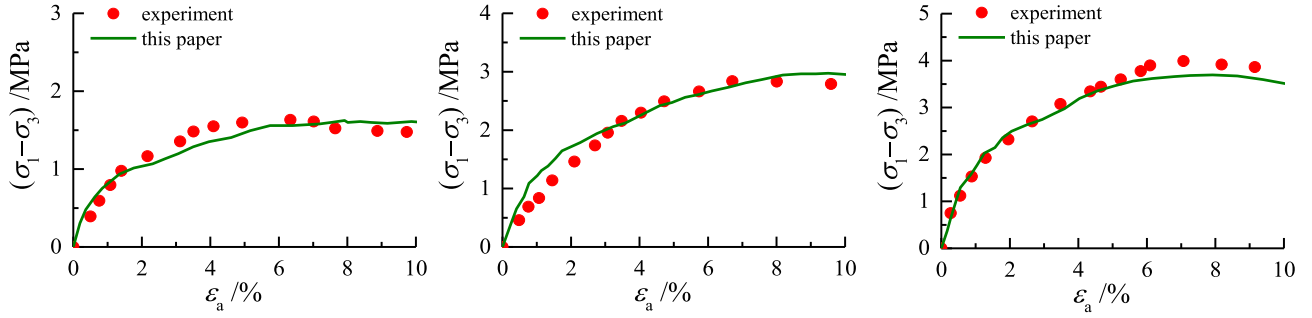


Fig. 6. The relationship between strain and deviatoric stress as obtained from a biaxial test.

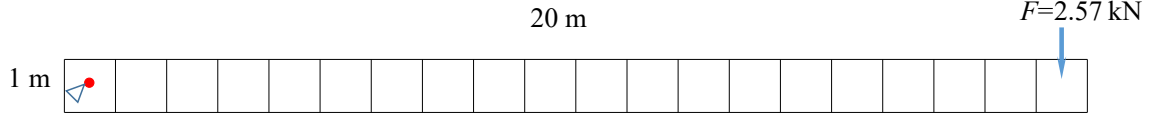


Fig. 7. The model of cantilever beam.

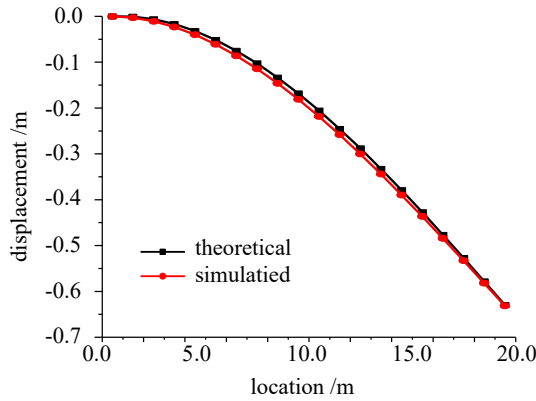


Fig. 8. The deflection of the beam.

and tangential contact stiffnesses between particles are each  $2.2 \times 10^8 \text{ N/m}$ , and the friction coefficient is 0.5. The normal stiffness of the contact between particles and walls is  $3 \times 10^8 \text{ N/m}$ , and the friction coefficient is 0.

Fig. 6 shows the axial strain  $\varepsilon_a$  and the deviatoric stress  $(\sigma_1 - \sigma_3)$  obtained from testing (Jiang et al., 2008) and simulation. The simulated results are in good agreement with the experimental results (Jiang et al., 2008). The deviatoric stress  $(\sigma_1 - \sigma_3)$  increases with the increase of confining pressure, and exhibits softening characteristics after reaching the peak stress. This example verifies the polygonal DEM program developed in this paper.

### 3.3. Continuum deformation simulation

Fig. 7 shows a 20 m long and 1 m high cantilever beam. The particles in the beam are connected by the proposed bond model with 10 springs. The normal modulus  $k_n$  of the bond model is 100 MPa and the tangential modulus is 40 MPa. A vertical constant load of 2.57 kN is applied to the centroid of the top particles. After the system is stabilized, the simulated deflection curve and the material mechanics solution are obtained, and as shown in Fig. 8, the results are in good agreement. The differences between the results come from the number of discrete particles and the number of spring set. This example demonstrates the correctness of the bond model developed in this paper.

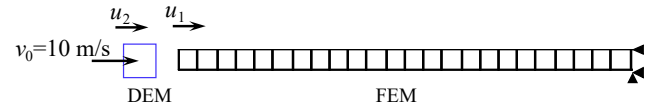


Fig. 9. Dynamic impact of a particle onto a prismatic bar.

### 3.4. Program verification

As shown in Fig. 9, a numerical simulation of the impact of rigid particles on an infinite prismatic bar (Fakhimi and Coetzee, 2009) is carried out. The rigid particles are simulated by DEM and the prismatic bar is simulated by FEM. The mass of the particles is  $0.0104\pi \text{ kg}$  and each have an initial horizontal velocity  $v_0$  of 10 m/s. For the prismatic bar, the physical parameters are as follows: sectional area of  $0.0004 \text{ m}^2$ , density of  $7800 \text{ kg/m}^3$ , elastic modulus of 210 GPa, and Poisson's ratio of 0. The normal contact stiffness and tangential contact stiffness are  $2 \times 10^7 \text{ N/m}$  and  $1 \times 10^7 \text{ N/m}$ , respectively.

Assuming that the particles are non-eccentrically impacted on the bar, the prismatic bar deforms only in the axial direction. The displacement of the left end of the bar is  $u_1$  and the displacement particle centroid is  $u_2$  during the impact process, respectively. The one-dimensional wave equation in the bar is.

$$\frac{\partial^2 u}{\partial t^2} = c^2 \frac{\partial^2 u}{\partial x^2} \quad (18)$$

where  $u$  is the displacement,  $t$  is the time, and  $c = \sqrt{E/\rho}$  is the longitudinal wave velocity of the bar. The general solution of the wave equation is.

$$u = f(x - ct) \quad (19)$$

The velocity at the left end is.

$$\dot{u}_1 = \frac{F}{\rho A c} \quad (20)$$

where  $F$  is the contact force, and  $A$  is the sectional area of the bar. Due to the conservation of linear momentum, the velocity of the rigid particle after impact is.

$$\dot{u}_2 = v_0 - \frac{1}{m} \int_0^t F dt \quad (21)$$

The overlapping rate of particles and bar during the time period of contact is.

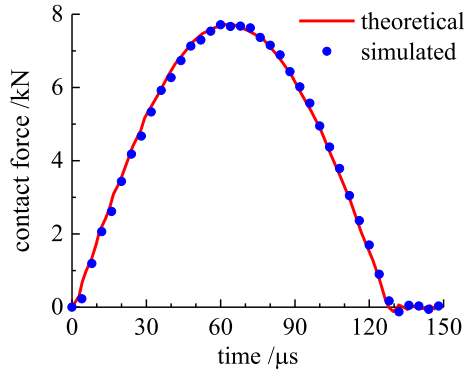


Fig. 10. The contact force of FEM bar.

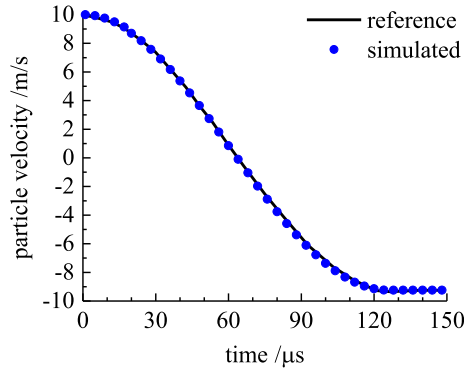


Fig. 11. The velocity of DEM particle.

$$\dot{\alpha} = \dot{u}_2 - \dot{u}_1 = v_0 - \frac{1}{m} \int_0^t F dt - \frac{F}{\rho A c} \quad (22)$$

Assuming that the normal contact stiffness of the particles with the bar is  $k_n$ , then,

$$\frac{\dot{F}}{k_n} = \dot{\alpha} = v_0 - \frac{1}{m} \int_0^t F dt - \frac{F}{\rho A c} \quad (23)$$

During the impact, the contact force  $F$  at  $t = 0$  is 0, and the solution (Goldsmith, 2001) of the above equation is,

$$F(t) = \beta e^{-qt} \sin(\omega t) \quad (24)$$

The history of contact force during the impact is shown in Fig. 10. The simulation results in this paper are in good agreement with the theoretical solution. The velocity of particles during the impact is shown in Fig. 11, which shows a good agreement of the results of this paper

with the theoretical results. According to equation (20), the velocity after impact is  $-9.245$  m/s, and the simulated result of this paper is  $-9.2448$  m/s (i.e. 0.002 % difference between simulation and analytical theory).

#### 4. Seismic damage analysis of CFRD

##### 4.1. DEM-FEM coupling model

A two-dimensional CFRD with a height of 100 m is used for analysis. The geometric parameters of the dam are shown in Fig. 12. The upstream slope and downstream slope of the dam are 1:1.4 and 1:1.65 respectively, and the width of the dam crest is 13 m. An U-shaped wave wall is set on the dam crest. The water depth is 96 m. The bedrock and dam are modeled by FEM and DEM respectively, and the interaction between dam and bedrock is simulated by the proposed DEM-FEM interface coupling method.

The large scale of the CFRD means that an excessive number of particles will be generated if the model follows the actual gradation curve. Therefore, while still following the gradation curve, particles below a certain size are discarded and their mass is evenly distributed to other particle groups. According to the enlarged gradation curve shown in Fig. 13, irregular polygonal particles with the number of edges between 4 and 8 are generated with sizes ranging between 150 mm and 2150 mm. The gradation curve for simulation is shown in Fig. 13, which is mostly consistent with the target curve. Compared with the main rockfill zone of the dam, the particle size range of the cushion zone is relatively narrow with a maximum particle size of 240 mm. There are a total of 158,000 polygonal particles in the model.

The face slab is discretized into rectangular particles with a length of 2 m as measured along the slope direction. The proposed bond model (i.

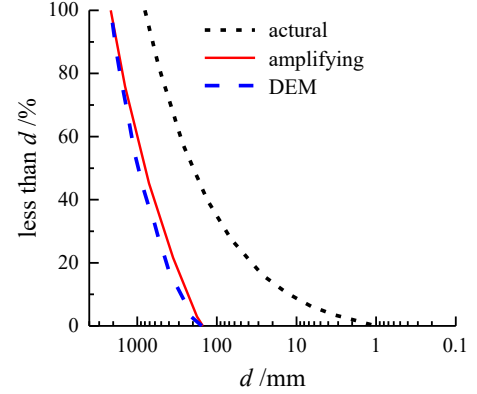


Fig. 13. The gradation curve of the rockfill.

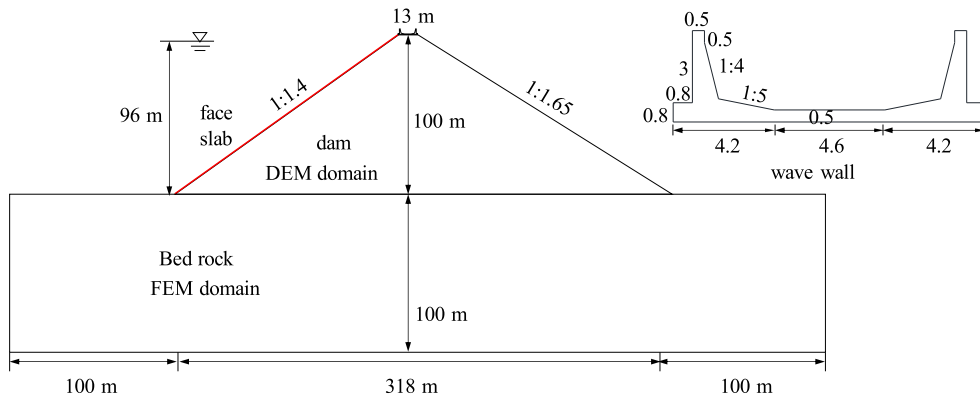


Fig. 12. The geometrical model of the CFRD.

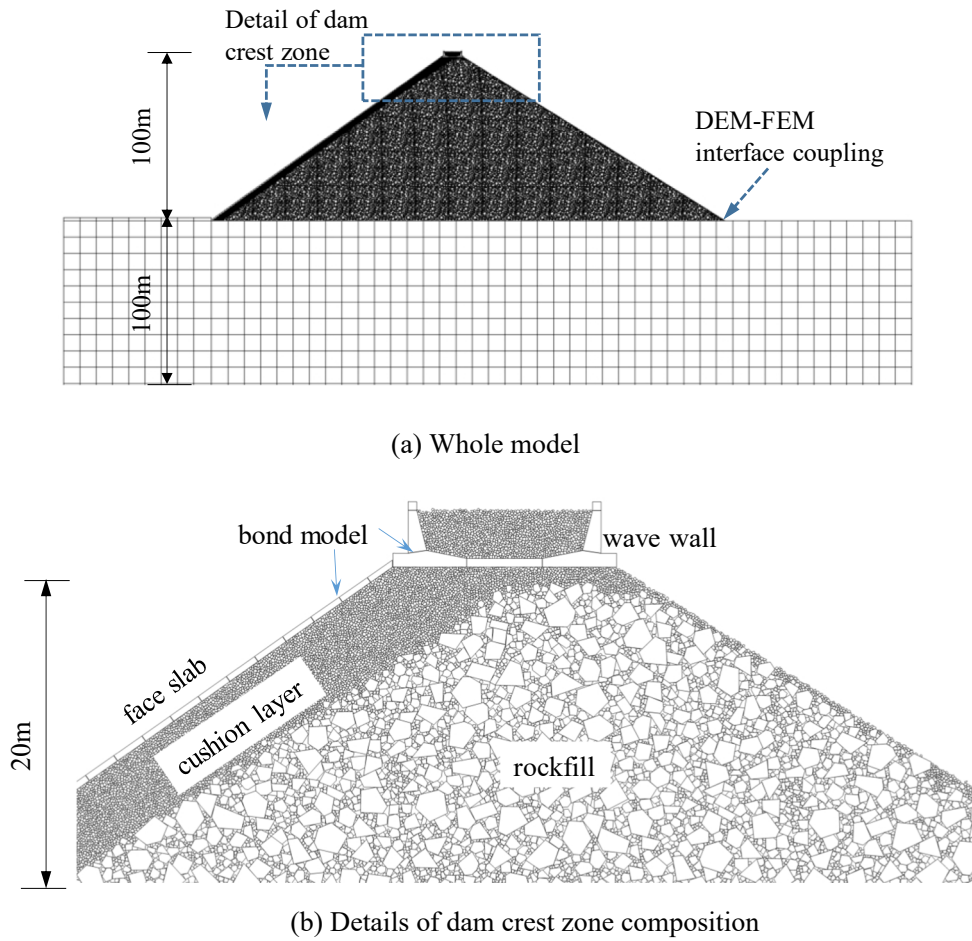


Fig. 14. The coupled DEM-FEM model of CFRD.

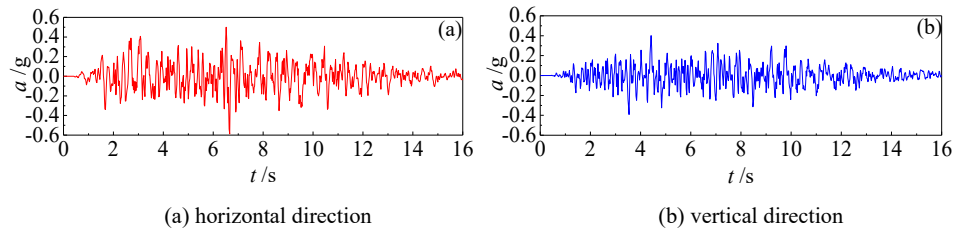


Fig. 15. The input groundmotion.

e. with 10 springs) is used to connect the particles along the slope direction. The wave wall experiences large displacements and small deformations during the earthquake, and can be simulated by rigid blocks. However, the program does not support such a complex particle shape; therefore, the wave wall is discretized into seven polygonal particles and connected to the 10 spring bond model. The final DEM-FEM coupling model is shown in Fig. 14.

The gravity and water pressure are considered to generate the initial contact forces between particles before earthquake. The concrete face slab has good impermeability and the downstream water level of CFRD is very shallow (Chen et al., 2018a; Wen and Li, 2020), therefore, the phreatic surface within CFRD drops rapidly after face slab. The effect of liquid phase and buoyancy in rockfill is limited and is not included in the study.

#### 4.2. Input ground motion

The non-uniform seismic wave input method as introduced in above is applied to describe the interaction between the dam and the foundation. The input ground motion is a simulated seismic wave based on the response spectrum obtained from the earthquake risk analysis of a CFRD. In the Wenchuan earthquake, the peak acceleration acting on the Zipingpu CFRD exceeded 0.5 g. Therefore, the peak ground accelerations (PGA) in the horizontal direction (along the river) and axial direction (perpendicular to the river) are 0.6 g, and the vertical PGA is 0.4 g. The acceleration time history and response spectrum of the seismic wave are shown in Fig. 15. The selected duration of seismic wave is 16.00 s.

#### 4.3. Calibration of microscopic parameters

The accuracy of the microscopic parameter in the DEM simulation

**Table 1**

Generalized plastic model parameters of rockfill.

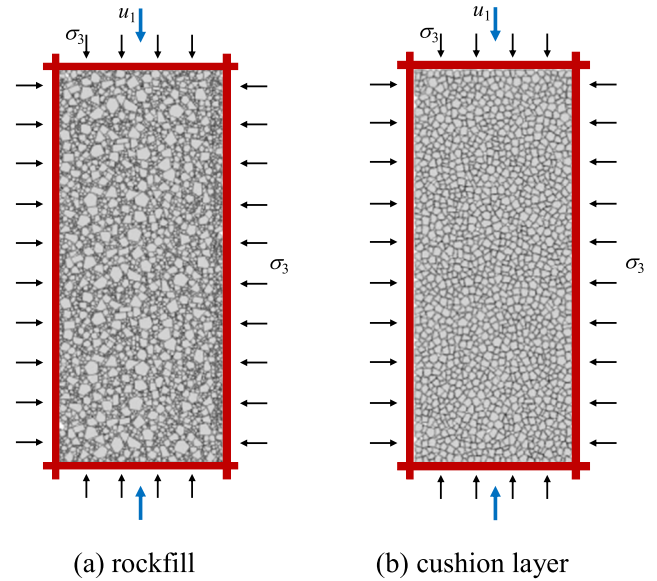
zone	$G_0$	$K_0$	$M_g$	$M_f$	$\alpha_f$	$\alpha_g$	$H_0$	$H_{U0}$	$m_s$
rockfill	965	1288	1.68	1.3	0.10	-0.4	550	1100	0.23
cushion layer	1021	1362	1.7	1.53	0.11	0.11	650	1300	0.44
zone	$m_v$	$m_l$	$m_u$	$r_d$	$\gamma_{DM}$	$\gamma_u$	$\beta_0$	$\beta_1$	
rockfill	0.44	0.5	0.5	110	50	5	30	0.025	
cushion layer	0.23	0.45	0.45	110	50	5	20	0.02	

determines whether the materials are modeled properly. Therefore, many researchers have studied the relationship between *meso*-parameters and macro-mechanical properties of geomaterials (Coetzee, 2017; Marigo and Stitt, 2015). However, there is no mature or recognized calibration method for determining the *meso*-parameters of DEM. At present, two kinds of methods are commonly used. One method is to directly measure the particle contact parameters at the mesoscopic level, and the other is to measure the macroscopic mechanical properties of particle aggregates, and then iteratively adjust the mesoscopic parameters until the simulated result is consistent with the macroscopic properties. At present, the second method is commonly used in geotechnical engineering. The macroscopic mechanical properties of geotechnical materials are measured by tests, and then the curve is identified by iteratively adjusting the mesoscopic parameters (Wang et al., 2007; Itasca, 2008).

For rockfill, laboratory triaxial tests are the most widely used method to obtain the macroscopic mechanical properties. Therefore, the triaxial test results can be used to calibrate the mesoscopic parameters for three-dimensional DEM analysis, but it is not applicable for two-dimensional analysis. Rockfill is a granular material; therefore, its mechanical properties are affected by confining pressure in three directions. The stress state of rockfill in triaxial test does not correspond to the two-dimensional DEM analysis. Currently, 2D DEM analyses in geotechnical engineering are mostly used in the numerical experimentation of material, and the focus is on the influence of mesoscopic parameters (e. g. particle size, particle shape, particle breakage, size composition, and so on) on macroscopic mechanical property (Alaei and Mahboubi, 2012; Gong et al., 2019; Manso et al., 2018; Nie et al., 2019; Zhang et al., 2020; Zhou and Song, 2016). These studies mainly investigate the influence of the changes in mesoscopic parameters on macroscopic characteristics. The theoretical parameters of regular particles or typical parameters can meet the requirements for conducting research. Therefore, it is not necessary to calibrate the mesoscopic parameters for rockfill of a practical CFRD project.

#### 4.3.1. Rockfill microscopic parameters

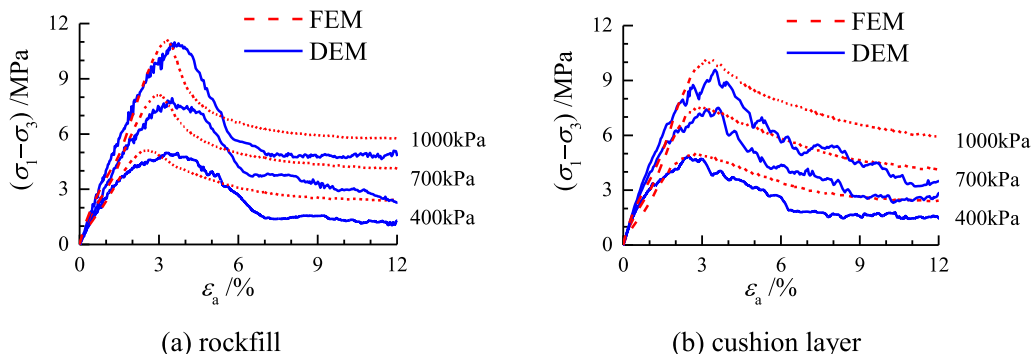
The purpose of this paper is to study the dynamic response of concrete face dams. The rockfill in two-dimensional simulations can experience plane strain. At the same time, the cross section of CFRDs are closer to the plane strain state. However, most laboratory tests of rockfill materials are currently triaxial tests. Such tests cannot be used to

**Fig. 17.** The biaxial compression test model of DEM simulation.

calibrate the *meso*-parameters for two-dimensional DEM.

The generalized plastic model of rockfill has been widely used in the static and dynamic analysis of rockfill dams, and the seismic damage of Zipingpu CFRD in Wenchuan earthquake has been well studied in literature and researchers have verified the ability of the model to describe the static and dynamic characteristics of rockfill. At the same time, the model parameters can be determined by fitting against data from conventional triaxial tests (Pastor et al., 1990; Zienkiewicz et al., 1998; Xu et al., 2012). Therefore, this paper calibrates the *meso*-parameters by means of the generalized plastic model of rockfill. The specific steps are:

- (1) The generalized plastic model parameters are calibrated according to the large triaxial rockfill test results;
- (2) The biaxial compression test is simulated via FEM and the generalized plastic model under the two-dimensional plane strain state;

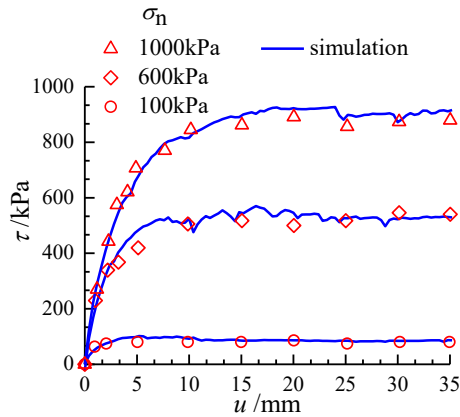
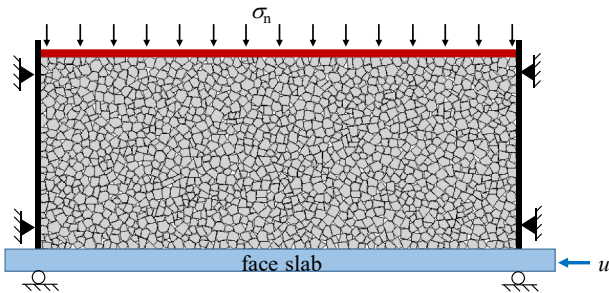
**Fig. 16.** The results of biaxial compression test simulation.



**Table 2**

The contact parameters of rockfill for DEM analysis.

zone	$\rho$ (kg/m <sup>3</sup> )	$k_n$ (N/m)	$k_s$ (N/m)	$\phi(^{\circ})$	$c$ (N)
rockfill	2700	$2.7 \times 10^8$	$2.0 \times 10^8$	51.6	0
cushion layer	2700	$6.0 \times 10^8$	$3.0 \times 10^8$	51.6	0

**Fig. 18.** The relationship between shear stress and displacement (Zhang and Zhang, 2008).**Fig. 19.** The DEM model of direct shear test of interface.

- (3) Two-dimensional DEM is used to simulate the biaxial compression test, and the results of step 2) are used to calibrate the *meso*-parameters;
- (4) DEM and FEM are used to simulate the response of the dam to verify the calibration parameters.

Based on the results obtained from the large-scale triaxial test, the parameters of the generalized plastic model for the rockfill and the cushion are calibrated, as listed in Table 1. Then the biaxial compression test under the plane strain state is simulated. The simulated confining pressures include 400 kPa, 700 kPa, and 1000 kPa. The simulation results are shown in Fig. 16. A DEM analysis model with a portion of the CFRD (Fig. 14) taken out as a biaxial test is used, as shown in Fig. 17. In the simulation, confining pressure is first applied in the vertical and horizontal directions, and deviatoric stress is applied after stabilization. The simulation results are shown in Fig. 16, and the corresponding *meso*-contact parameters are listed in Table 2.

#### 4.3.2. Micro-parameters of contact between panel and cushion

The mechanical properties of the soil-structure interface are mainly related to the normal stress, which is similar to the state of the two-dimensional DEM analysis. Therefore, the *meso*parameters of the interface between the face slab and the cushion are calibrated by the direct shear test of the interface. Zhang and Zhang (2008) carried out a direct shear test on the face slab and cushion material of the Zipingpu

**Table 3**

Contact parameters between cushion and slab.

$\rho$ (kg/m <sup>3</sup> )	$k_n$ (N/m)	$k_s$ (N/m)	$\phi(^{\circ})$	$c$ (N)
2700	$1 \times 10^9$	$8 \times 10^8$	48.7	2000

CFRD, and the results are shown in Fig. 18.

The cushion zone of the face rockfill dam is used as the DEM analysis model, as shown in Fig. 19. The normal stresses include 100 kPa, 600 kPa and 1000 kPa, respectively. The left and right sides are constrained. The normal stresses are applied on the top of the model and horizontal displacement is applied at the bottom panel after stabilization. The simulated shear stress and shear displacement are shown in Fig. 18, which are in good agreement with the experimental results. The *meso*-parameters of the interface between the face slab and the cushion are listed in Table 3.

#### 4.3.3. Parameter verification

In order to verify the *meso*parameters, an FEM analysis based on the generalized plastic model and a DEM analysis of the seismic response of the two-dimensional CFRD are carried out. The emphasis lay on this section is to verify the *meso*parameters, therefore, the moderate earthquake excitation is adopted and the PGAs along the river and in vertical direction are adjusted to 0.3 g and 0.2 g, respectively. The model shown in Fig. 15 (excluding the wave wall and foundation) is used for DEM analysis. The geometry and size of the finite element model is the same as that of the DEM analysis model.

The earthquake-induced residual deformations of the dam computed through FEM are shown in Fig. 20, which shows that the maximum longitudinal and vertical displacements are 0.65 m and 0.33 m, respectively. The results computed through DEM are shown in Fig. 21, which shows that the maximum along-river and vertical displacements are 0.55 m and 0.28 m, respectively. The results obtained from DEM agree well with those obtained from FEM, which demonstrates it is feasible to analyze the seismic response of a CFRD by using calibrated *micro*parameters.

#### 4.4. Seismic failure analysis of CFRD

In this section, the seismic failure analysis of the CFRD is carried out using DEM. The contact parameters of rockfill and cushion are listed in Table 2, and the contact parameters between cushion and slabs are listed in Table 3. The bond model of face slab and wall is assumed to follow concrete behavior with  $k_n = 31.0$  GPa and  $k_s = 13.28$  GPa.

##### 4.4.1. Dam deformation

The residual deformations of the dam body are shown in Fig. 22. The results indicate that the initial failure of the CFRD under the earthquake occurs in the top zone (i.e. the crest of the dam and the upper part of the downstream slope). The deformation vectors of the top zone are shown in Fig. 22(c).

There is pronounced slipping towards the downstream direction from the top zone, and the vectors generally follow a circular arc or an elliptical arc. Meanwhile, there are large displacement vectors parallel to the slope at the downstream slope, indicating that some rocks may roll on the downstream slope during a strong earthquake.

In order to study the seismic failure process and failure mode of the top zone, the deformations at several moments are plotted in Fig. 23. The displacement time history at the middle of the dam crest and at the top of the downstream slope are shown in Fig. 24. During the earthquake, failure initiated at the top zone and lead to the following failure mode:

- 1) Loosening, slipping, and even rolling of shallow rockfill in the upper part of the downstream slope and settlement of the dam crest, but no obvious slip surface;

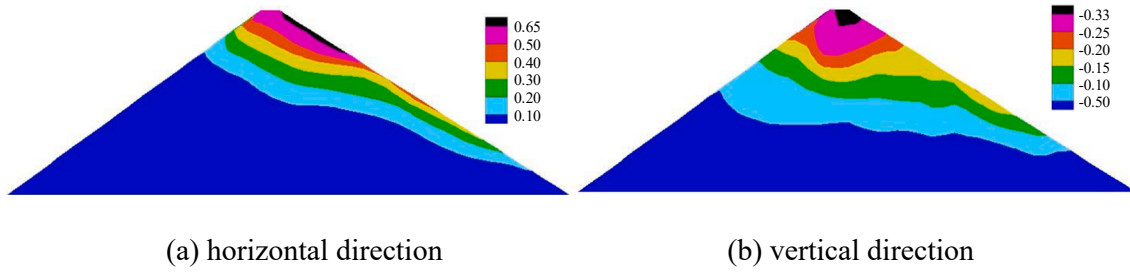


Fig. 20. Residual deformations after earthquake as computed via FEM(unit: m).

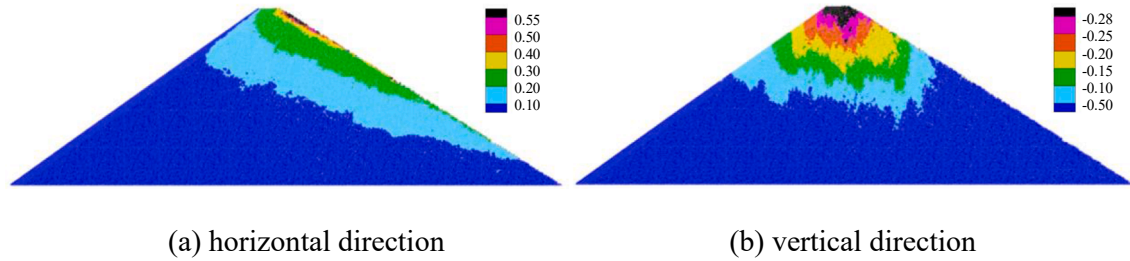


Fig. 21. Residual deformations after earthquake as computed via DEM (unit: m).

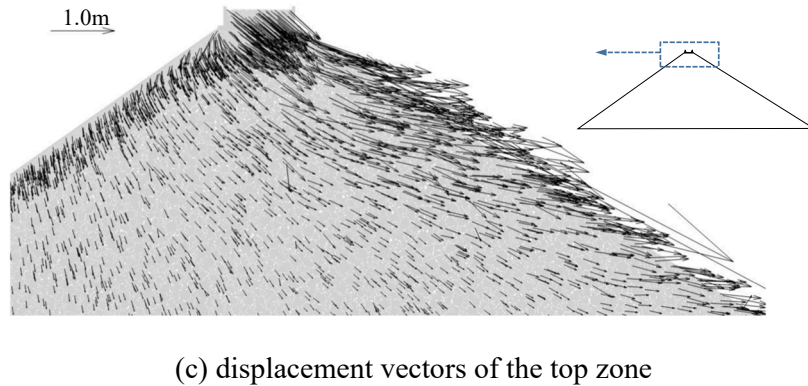
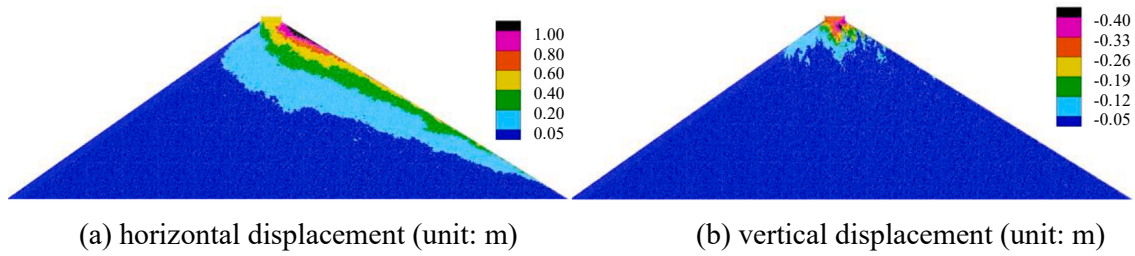


Fig. 22. Post-earthquake residual deformations.

- 2) Separation between concrete face slab and the rockfill, downstream slipping of the wave wall, and separation between the wave wall and the concrete face slab.

After the earthquake, the settlement at the top of the dam is 0.41 m, the horizontal displacement at the middle of dam crest is 0.64 m, and the maximum horizontal displacement of the dam is 1.08 m at the top of downstream slope.

In the Wenchuan earthquake, the failure of the crest and the upper part of the downstream slope of the Zipingpu CFRD (Kong, 2015; Zhang et al., 2015) includes settlement, loosening, rock rolling (as shown in Fig. 25), and the separation between the wave wall and the concrete face

slab. The seismic failure mode of the CFRD during a shaking table test is shown in Fig. 26. These results from field investigation and laboratory tests verify the simulation results in this paper. The DEM-FEM coupling analysis in this paper intuitively reproduces the initial failure mode and damage evolution of the CFRD during earthquake excitation.

#### 4.4.2. Wave wall displacement

The displacement history of the wave wall under earthquake is shown in Fig. 27. The upstream slope of the dam is protected by the concrete face slab. Thus, the deformation of the upstream side is smaller than that of the downstream side. The wave wall is located on the rockfill, and its settlement is determined by the deformation of the dam.

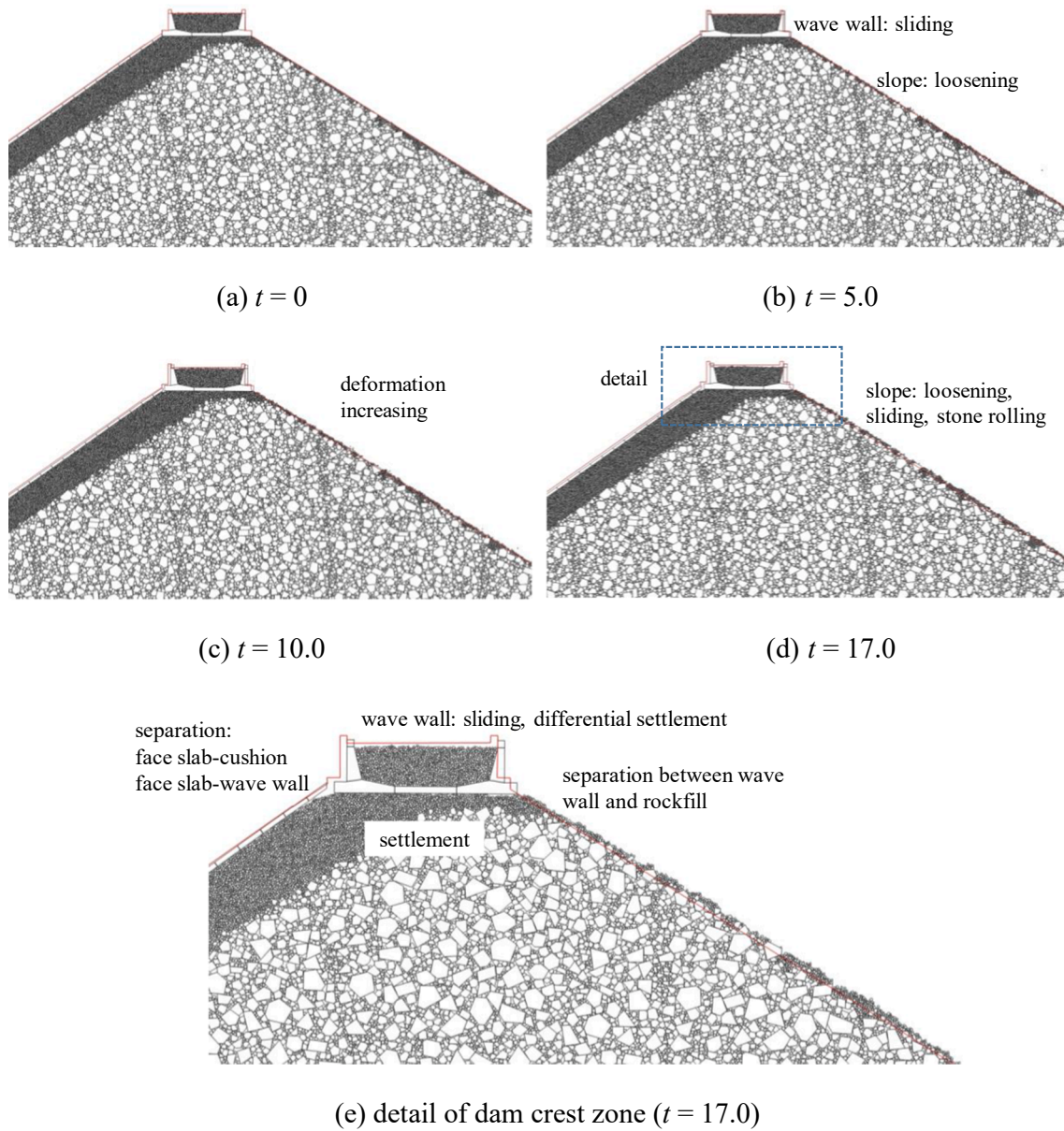


Fig. 23. Deformation of middle-upper part of dam during an earthquake.

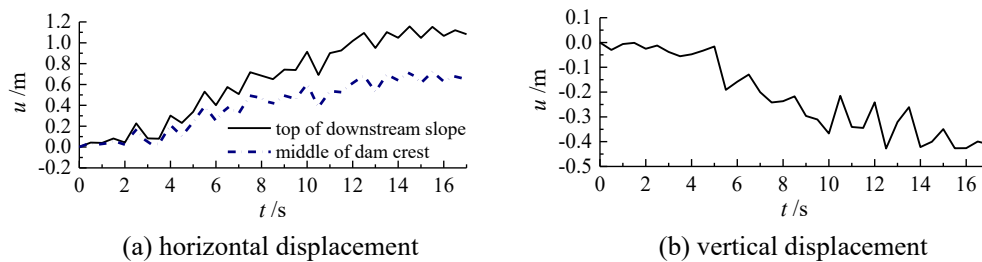


Fig. 24. History of deformation at the dam crest during an earthquake.

Therefore, the wave wall experiences differential settlement with a smaller upstream and larger downstream. The settlements of the upstream side and downstream side of the wave wall after the earthquake are 0.26 m and 0.32 m, respectively, as shown in Fig. 27(a). The horizontal displacements of the wave wall are shown in Fig. 27(b). During the earthquake, the wall displaces horizontally towards the downstream

direction, cumulating in a final displacement of 0.55 m. The horizontal displacement of the face slab is limited by the support of rockfill. Therefore, the gap between slab and wave wall gradually increases. The residual gap after the earthquake is 0.51 m, as shown in Fig. 27(c).



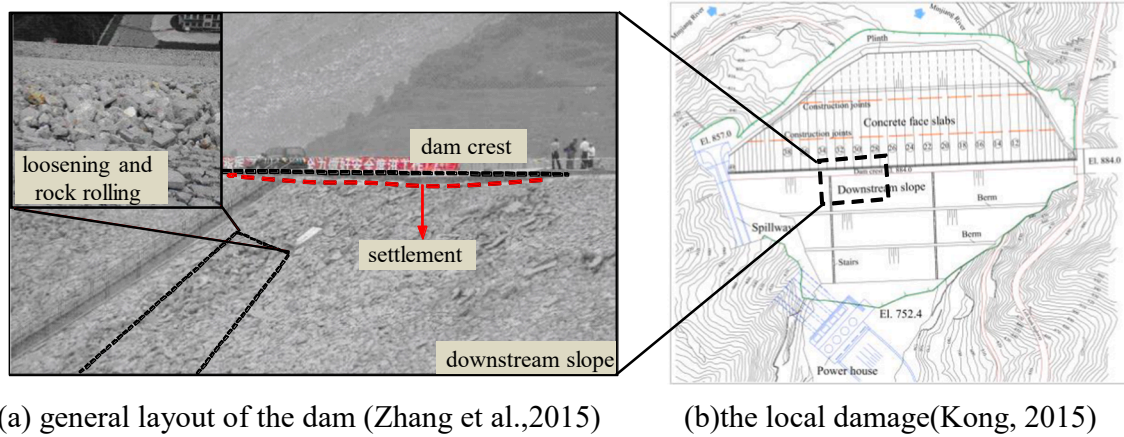


Fig. 25. Earthquake induced damage observed in the Zipingpu CFRD.

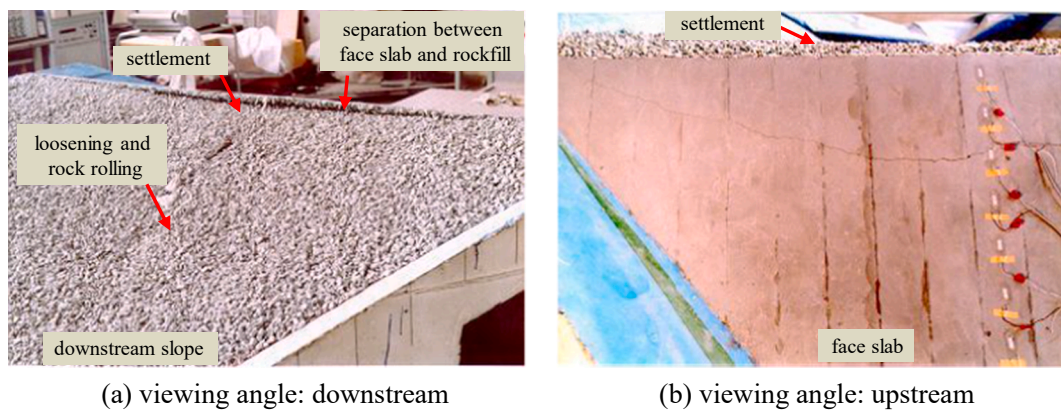


Fig. 26. The seismic failure mode of CFRD during shaking table test (Kong, 2015).

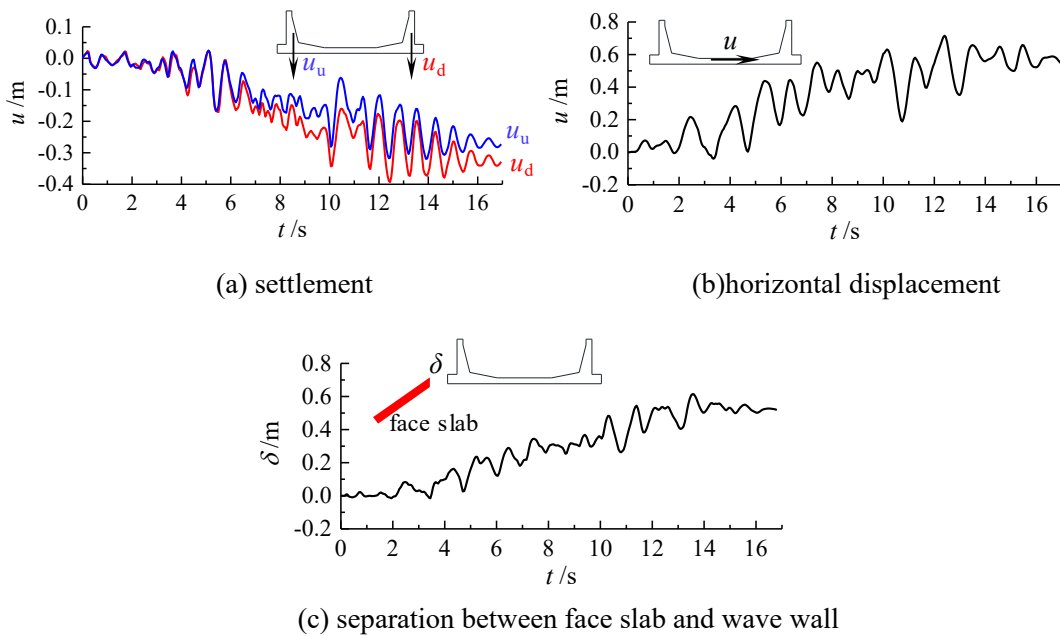


Fig. 27. The response of the wave wall during the earthquake.



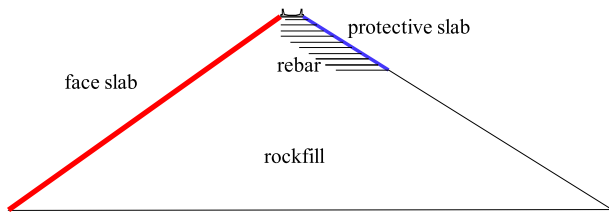


Fig. 28. Schematic diagram of strengthening dam slope using nailed protective slab.

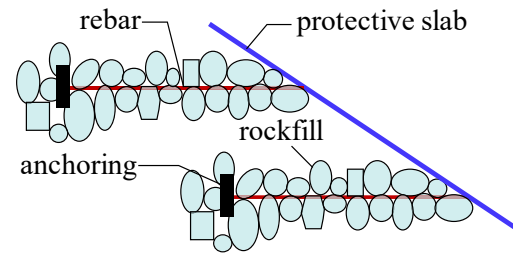
## 5. Effective analysis of anti-seismic measures

### 5.1. anti-seismic measure of nailed protective surface

According to the results of the previous section, the initial failure modes of the CFRD include loosening, slipping, and rolling of rocks from the rockfill and the shallow sliding of the dam slope at top zone. Therefore, the key towards implementing effective anti-seismic measures is to reduce the deformation of the rockfill. Reinforcement anchorage can significantly improve the strength and stability of structures and has been widely used in foundation pits, railways, highways, retaining walls and hydraulic structures. The main materials used



(a) construction process



(b) connection mode

Fig. 29. Schematic diagram of nailed protective slab.

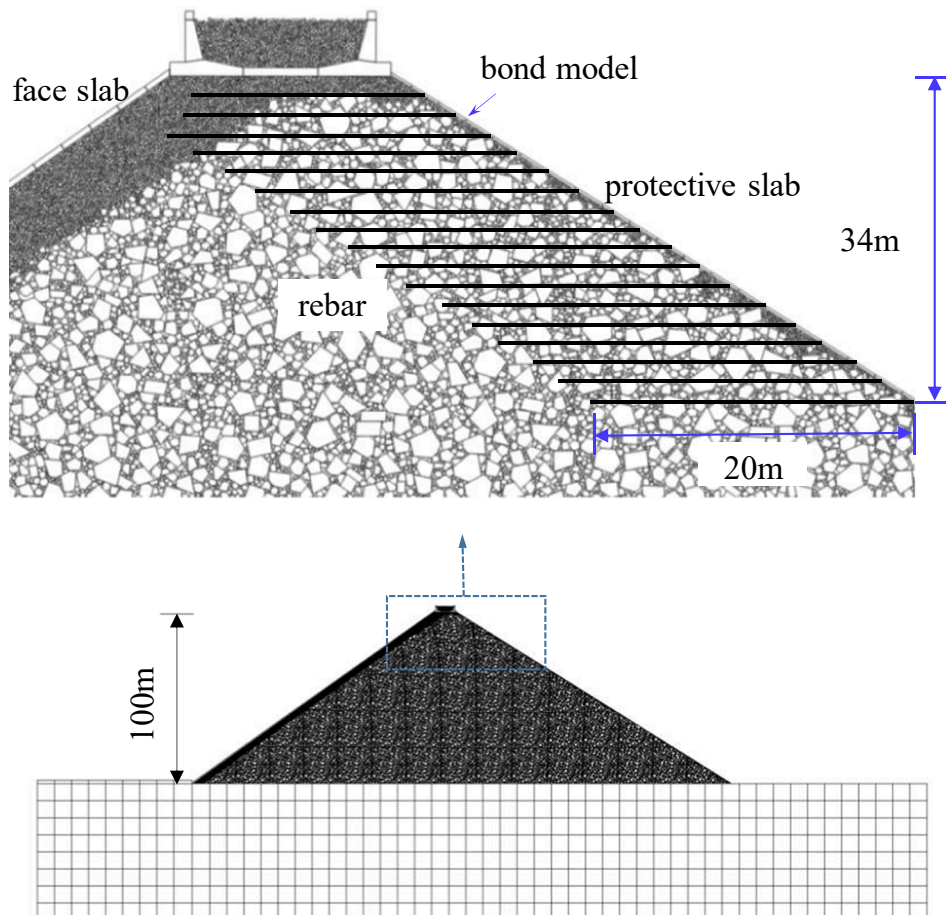


Fig. 30. The coupled analysis model of CFRD with anti-seismic measure (dam crest zone).

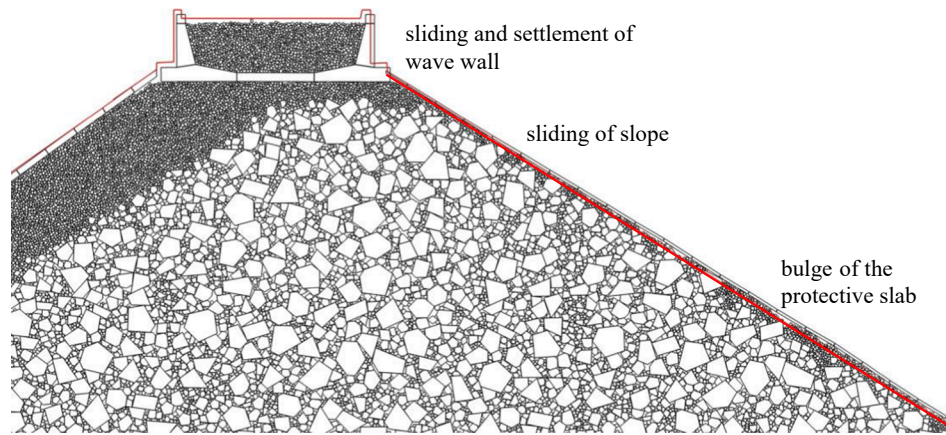


Fig. 31. The deformation pattern of dam crest zone with anti-seismic measure.

for reinforcement anchorage include anchors, steel, geotextiles, geogrids and geocells. Based on failure mode and characteristics of the earth-rock dam as observed from a shaking table model test, Kong (2015) proposed anti-seismic measures of the body comprising of a nailed protective slab, as shown in Fig. 28. In the application, the protective slab consists of reinforcement fabric and spray cement mortar, and is set in the middle and upper part of the dam slope to limit the looseness and slippage of the rockfill. At the same time, the protective panel is anchored to the interior body by the reinforcement (Fig. 29) so that the protective slab and the rockfill become a whole, and the reinforcement becomes more effective.

The nailed protective slab has been applied in Jilintai CFRD and as

well as other earth-rock dams. However, the safety factor of the slope is currently evaluated based on the rigid limit equilibrium method (Dong and He, 2019; Zou et al., 2009), which separates the relationship between dynamic response and the deformations of the sliding body. Therefore, this section uses DEM to verify and quantitatively evaluate the effect of nailed protective slabs for further engineering applications.

## 5.2. Computational models and parameters

Using the initial failure analysis results as a guide, a nailed protective slab is set to protect the downstream slope over the upper 2/3 dam

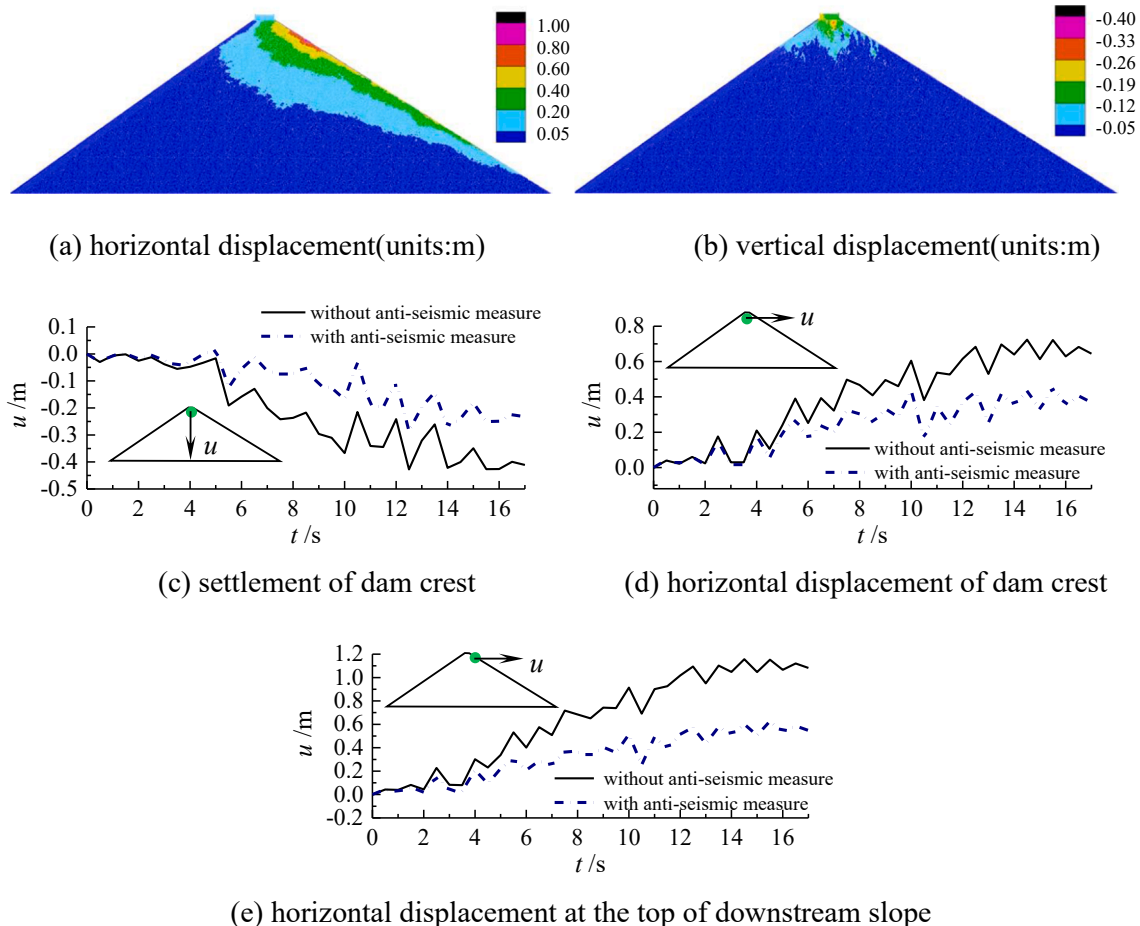


Fig. 32. The residual deformation of dam with anti-seismic measure.

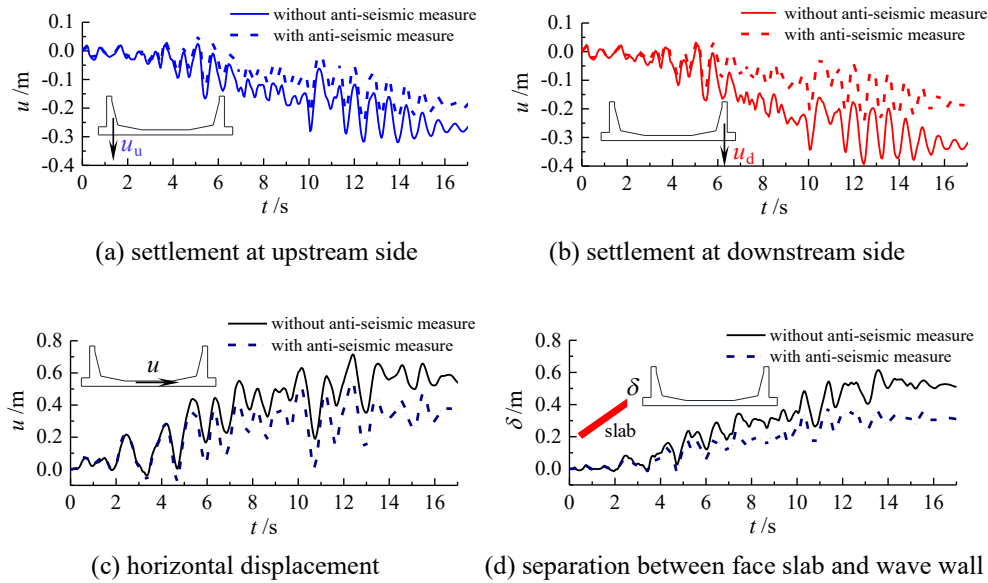


Fig. 33. The displacement of wave wall with anti-seismic measure.

height (Fig. 30). The thickness of the slab is 10 cm, and is discretized as rectangular particles and connected by the bond model to simulate the deformation characteristics. Rebars are simulated by bar elements. The maximum length of the rebar is 20 m, and the vertical spacing is 2 m.

The parameters of rebar are as follows: density is  $7800 \text{ kg/m}^3$ , elastic modulus is 200 GPa, tensile strength is 400 MPa, area is  $2.56 \text{ cm}^2$ . The parameters of the protective slab are as follows: density is  $2400 \text{ kg/m}^3$ , elastic modulus is 550 MPa, Poisson's ratio is 0.2. The protective slab is composed of sprayed cement mortar outside the reinforcement fabric, which is regarded as a flexible protective material. The failure characteristics of the fabric are not considered during the earthquake. In the simulation, the rebar is in an overlapping mesh with the discrete elements, which can interact with each other, as shown in Fig. 30.

### 5.3. Effect of anti-seismic measures

#### 5.3.1. Dam deformation

The post-earthquake deformation of the dam crest area with anti-seismic measures is shown in Fig. 31. The deformation mode of dam body is the settlement of the dam crest, the slipping of the downstream slope, and the bulging of the protective slab. The wave wall slips downstream, resulting in the separation away from the face slab, but not from the rockfill.

The deformations of the dam after earthquake excitation are shown in Fig. 32(a) and (b), and the time histories of the horizontal and vertical displacements of the downstream slope crest and dam crest are respectively shown in Fig. 32(c) and (d). After adopting anti-seismic measures, the maximum horizontal displacement occurs in the middle and upper part of the downstream slope, which decreases from 1.08 m to 0.84 m (i.e. reduction of 22 %). The settlement in the middle of the dam crest decreased from 0.41 m to 0.23 m (i.e. reduction of 44 %), and the displacement along the river in the middle of the dam crest decreased from 0.64 m to 0.37 m (i.e. reduction of 42 %). The displacement along the river at the top of the downstream slope decreased from 1.08 m to 0.55 m (i.e. reduction of 49 %).

#### 5.3.2. Wave wall displacement

The displacement history of the wave wall during the earthquake is shown in Fig. 33. The residual deformations of the dam decreased after implementing anti-seismic measures. Thus, the seismic response of the wave wall is weakened and as a result, there is almost no differential settlement of the wave wall.

Table 4

The influence of anti-seismic measure on wave wall response.

Case	Settlement/m		Horizontal displacement/m	Separation between face slab and wave wall/m
	upstream	downstream		
Without anti-seismic measure	0.26	0.32	0.55	0.51
With anti-seismic measure	0.19	0.20	0.33	0.30

The displacement of the wave walls before and after seismic measures is summarized in Table 4. After implementing seismic measures, the settlement of the upstream side is reduced from 0.26 m to 0.19 m (i.e. 27 % reduction); the settlement of downstream side is reduced from 0.32 m to 0.20 m (i.e. 38 % reduction); the horizontal displacement is reduced from 0.55 m to 0.33 m (i.e. 40 % reduction); the gap with panel is reduced from 0.51 m to 0.30 m (i.e. 41 % reduction). The nailed protective slab effectively reduced the deformations of the dam and the displacements of the wave wall, thereby demonstrating good anti-seismic capabilities.

## 6. Conclusion

In this paper, a custom, polygonal DEM-FEM interface coupling multi-scale analysis program under the same solving framework is developed and firstly introduced to the failure analysis of high CFRD under strong earthquake. The initial failure characteristics is studied, and the effect of anti-seismic measures is quantified.

- (1) The polygonal DEM is applied to describe the strong-nonlinearity and discontinuous of dam. The particle shape and grading of cushion and rockfill are considered. The FEM and non-uniform seismic wave input method is combined to simulate the interaction between dam and foundation. A bonded model is proposed to describe the deformation characteristics of face slab and anti-seismic measure. On this basis, a refined multi-scale analysis model of CFRD is established and applied to investigate the seismic failure characteristics.

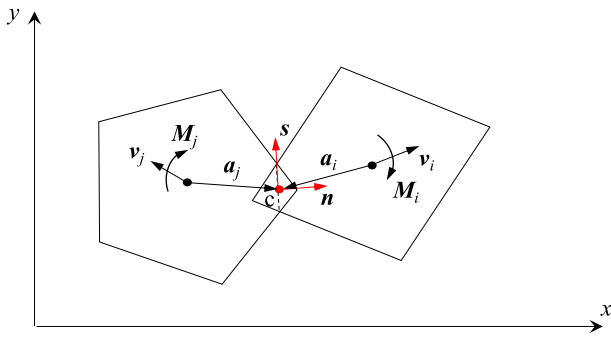


Fig. A1. The contact of polygon element.

- (2) Under earthquake excitation, the initial failure of CFRD occurs at the top zone of the dam (i.e. the dam crest and the upper part of the downstream slope). Failure characterized by the loosening, sliding and even rolling away of the shallow rockfill on the slope. Failure further presents as settlement of the dam crest, separation between the face slab and the rockfill, downstream sliding of the wave wall and the separation of the wave wall from the face slab. The analysis method intuitively reproduces the initial seismic failure mode and failure evolution of the CFRD.
- (3) The effect of the anti-seismic measures (i.e. nailed protective slab installed at the upper part of the downstream slope) for dam is verified and quantified. With the anti-seismic measures, the integrity of the top zone improved, resulting in substantial damage mitigation. The maximum displacement of the dam along the river occurred further downslope, and the displacement decreased by 35 %. At the same time, the vertical displacement in the middle of the dam crest decreased by 44 % and the settlement of the wave wall reduced by 27 %. The horizontal displacement also reduced by 40 % while the separation between the face slab and wave wall reduced by 41 %. The nailed slab greatly reduced dam deformation and the displacement of the wave wall, and can be used as an effective anti-seismic measure.

- (4) The proposed method can investigate the failure characteristics and quantify the effect of the anti-seismic measure. The method overcomes the limitations of traditional continuum analyses on the strong-nonlinearity, large deformation and discontinuous of strong earthquakes damage. It provides an effective way for further analysis of the break for rockfill dams, and can be applied to the seismic failure analyses of other geotechnical engineering.

#### CRediT authorship contribution statement

**Yongqian Qu:** Software, Methodology, Formal analysis, Investigation, Data curation, Writing – original draft, Visualization, Funding acquisition. **Degao Zou:** Conceptualization, Software, Methodology, Project administration, Funding acquisition. **Jingmao Liu:** Validation, Resources. **Zhikai Yang:** Writing – original draft. **Kai Chen:** Validation, Writing – review & editing.

#### Declaration of Competing Interest

The authors declare that they have no known competing financial interests or personal relationships that could have appeared to influence the work reported in this paper.

#### Data availability

The authors do not have permission to share data.

#### Acknowledgements

The research work described in this paper was supported by the National Natural Science Foundation of China (Grant Nos. 52192674, U1965206 and 52109151) and the China Postdoctoral Science Foundation (Grant Nos. BX20200074 and 2021M690520). The writers would like to greatly acknowledge all the financial support and express their sincerest gratitude.

## Appendix A. . Discrete element method

For two contacting particles  $i$  and  $j$ , as shown in Fig. 1, the contact force of particle  $i$  from particle  $j$  can be divided into normal force, tangential force and the torque. The calculation is described below.

### (1) Normal force.

The simplest way to calculate the normal force is the linear contact model. With consideration to the degree of embedment and energy dissipation, the normal contact force  $f_n$  is.

$$f_n = k_n \delta_n - \gamma_n \Delta v_n \quad (A1)$$

where  $k_n$  is the contact stiffness,  $\delta_n$  is the length of overlap,  $\gamma_n$  is the normal viscous damping coefficient and  $\Delta v_n$  is the normal component of relative velocity of two particles. For circular or spherical particles, the contact point is on the connection line between the center of the circle or sphere; thus, the rotation does not cause normal relative velocity.

$$\Delta v_n = (\mathbf{v}_i - \mathbf{v}_j) \cdot \mathbf{n} \quad (A2)$$

where  $\mathbf{n}$  is the normal direction of the contact force. However, for polygonal particles, the normal direction of the contact force is not necessarily line connecting the centroids of the particles but is rather defined as the vertical direction to the line of intersection points. The midpoint  $c$  of the connection line is the point of contact force. Therefore, the rotation will generate relative velocity in the normal direction.

$$\Delta v_n = \Delta \mathbf{v}_{ij} \cdot \mathbf{n} \quad (A3)$$

$$\Delta \mathbf{v}_{ij} = \mathbf{v}_i - \mathbf{v}_j + \boldsymbol{\omega}_i \times \mathbf{a}_i + \boldsymbol{\omega}_j \times \mathbf{a}_j \quad (A4)$$

where  $\mathbf{v}_i$  and  $\mathbf{v}_j$  are the translational velocity vectors at the barycenter of particles  $i$  and  $j$ ,  $\boldsymbol{\omega}_i$  and  $\boldsymbol{\omega}_j$  are the rotational velocity vectors around the barycenter of particles  $i$  and  $j$ ,  $\mathbf{a}_i$  and  $\mathbf{a}_j$  are the radius vectors from the barycenter of particles  $i$  and  $j$  to the contact point, and  $\Delta \mathbf{v}_{ij}$  is the velocity vector of particles  $i$  relative to particles  $j$ .

### (2) Tangential force.

The relative tangential velocity of contact point  $\mathbf{v}_s$  is.

$$\mathbf{v}_s = \mathbf{v}_{ij} - \mathbf{n} (\mathbf{n} \cdot \mathbf{v}_{ij}) \quad (A5)$$



Since tangential force is related to motion state and loading history, it is appropriate to express it in incremental form,

$$\Delta f_s = k_s \Delta u_s - \gamma_s \Delta v_s = k_s \Delta v_s \Delta t - \gamma_s \Delta v_s \quad (A6)$$

$$f_s = f_s^{old} + \Delta f_s \quad (A7)$$

where  $k_s$  is the tangential contact stiffness,  $\Delta u_s$  is the sliding increment,  $\gamma_s$  is the tangential viscous damping coefficient, and  $\Delta t$  is the time step,  $f_s^{old}$  is the tangential contact force of the last time step.

From the Mohr-Coulomb criterion, the maximum tangential force is.

$$|f_s| \leq c + f_n \tan \varphi \quad (A8)$$

where  $\varphi$  is the friction angle and  $c$  is the cohesive force. The cohesion is shear impedance rather than tensile impedance and is constant during simulation.

(3) Rotation impedance.

The rotational impedance is a paired couple acting on the particles preventing the rotation of the particles. The relative rotational velocity at the contact point is.

$$\Delta v_r = -\omega_i \times a_i + \omega_j \times a_j \quad (A9)$$

Rotational impedance torque increment is.

$$\Delta M_r = k_r \Delta \theta_r - \gamma_r \Delta v_r = k_r \Delta v_r \Delta t - \gamma_r \Delta v_r \quad (10)$$

$$M_r = M_r^{old} + \Delta M_r \quad (11)$$

where  $k_r$  is the anti-rotational stiffness,  $\Delta \theta_r$  is the relative rotation angle increment,  $\gamma_r$  is the rotational viscous damping coefficient,  $f_s^{old}$  is the rotational impedance torque of the last time step.

Similar to the tangential contact force, assuming that the rotation also follows the Mohr-Coulomb criterion, the maximum rotational impedance torque is.

$$|M_r| \leq \eta f_n \quad (12)$$

where  $\eta$  is anti-rotation coefficient and are in units of length.

(4) Damping.

In Rayleigh theory, the damping force contains both stiffness damping and mass damping. The stiffness damping is equivalent to the damper that prevents the particles from moving relative to each other when the particles are in contact, and its influence is reflected in the contact force and rotational impedance. The mass damping is considered as a series of viscous dampers acting on the barycenter of the particles, thereby reducing particle motion and dissipating the kinetic energy of the particles. The direction of the mass damping force is opposite to the direction of the velocity, and the magnitude is proportional to the mass and velocity. The translational and rotational mass damping forces are.

$$C_i = -\alpha m_i v_i \quad (13)$$

$$q_i = -\alpha_r I_i \ddot{\theta}_i \quad (14)$$

where  $C_i$  is the translational damping force of particle  $i$ ,  $\alpha$  is the damping coefficient,  $m_i$  is the mass of particle  $i$ ,  $q_i$  is the rotational damping moment of particle  $i$ ,  $\alpha_r$  is the rotational damping coefficient, and  $I_i$  is the moment of inertia of particle  $i$ .

The resultant force and moment of particle  $i$  are.

$$F_i = \sum_j (f_{jn} n + f_{js} s) + C_i + F_i^{ext} \quad (15)$$

$$M_i = \sum_j [a_i \times (f_{jn} n + f_{js} s) + M_r] + q_i + M_i^{ext} \quad (16)$$

where  $F_i^{ext}$  is the external force on particle  $i$  and  $M_i^{ext}$  is the external torque on particle  $i$ .

## References

- Alaei, E., Mahboubi, A., 2012. A discrete model for simulating shear strength and deformation behaviour of rockfill material, considering the particle breakage phenomenon. *Granular Matter* 14 (6), 707–717.
- Boulanger, R.W., Bray, J.D., Merry, S.M., et al., 1995. Three-dimensional dynamic response analyses of Cogswell Dam. *Can. Geotech. J.* 32 (3), 452–464.
- Chen, K., Zou, D., Kong, X., et al., 2018a. Global concurrent cross-scale nonlinear analysis approach of complex CFRD systems considering dynamic impervious panel-rockfill material-foundation interactions. *Soil Dyn. Earthquake Eng.* 114, 51–68.
- Coetzee, C.J., 2017. Review: Calibration of the discrete element method. *Powder Technol.* 310, 104–142.
- Cundall, P.A., Strack, O.D.L., 1979. A discrete numerical model for granular assemblies. *Geotechnique* 29 (1), 47–65.
- Deluzarche, R., Cambou, B., 2006. Discrete numerical modelling of rockfill dams. *Int. J. Numer. Anal. Meth. Geomech.* 30 (11), 1075–1096.
- Dong, G.Q., He, L., 2019. Study on nailing seismic reinforcement measures for slope protection face slab of high dam. *YELLOW RIVER*. 41 (11), 144–146 in Chinese.
- Fakhimi, A., Coetzee, C.J., 2009. A hybrid discrete-finite element model for numerical simulation of geomaterials Review: Calibration of the discrete element method. *Computers and Geotechnics. Powder Technol.* 36 310(3), 386–395.
- Goldsmith, W., 2001. Impact, the theory and physical behavior of colliding solids. Dover Publications INC, New York.
- Gong, J., Liu, J., Cui, L., 2019. Shear behaviors of granular mixtures of gravel-shaped coarse and spherical fine particles investigated via discrete element method. *Powder Technol.* 353, 178–194.
- Itasca, C.G.I., 2008. Pfc3d (particle flow code in 3 dimensions), version 4.0. ICG, Minneapolis.
- Jiang, J.S., Chen, Z.L., Jiang, X.L., 2008. Two-dimensional model test for coarse-grained soil. *J. Yangtze River Sci. Res. Inst.* 02, 38–41 (in Chinese).
- Kartal, M.E., Bayraktar, A., Başağa, H.B., 2010. Seismic failure probability of concrete slab on CFR dams with welded and friction contacts by response surface method. *Soil Dyn. Earthquake Eng.* 30 (11), 1383–1399.
- Kh, A.B., Mirghasemi, A.A., Mohammadi, S., 2011. Numerical simulation of particle breakage of angular particles using combined DEM and FEM. *Powder Technol.* 205 (1–3), 15–29.

- Kim, Y., Kim, B., 2008. Prediction of relative crest settlement of concrete-faced rockfill dams analyzed using an artificial neural network model. *Comput. Geotech.* 35 (3), 313–322.
- Kong, X.J., 2015. Seismic performance of concrete face rockfill dam. Science Press, Beijing (in Chinese).
- Kong X J, Zhou C G, Zou D G, et al., 2019. Influence of the dynamic interaction between high rockfill dam and foundation. *Journal of Hydraulic Engineering*, 2019,50(12): 1417-1432.
- Kong, X.J., Liu, J.M., Zou, D.G., 2016. Numerical simulation of the separation between concrete face slabs and cushion layer of Zipingpu dam during the Wenchuan earthquake. *Science China-technological Sciences*. 59 (4), 531–539.
- Liu, C., 2021. Matrix discrete element analysis of geological and geotechnical engineering. Springer.
- Liu, J., Du, Y., Du, X., et al., 2006. 3D viscous-spring artificial boundary in time domain. *Earthquake Engineering and Engineering Vibration*, 2006, 5(1):93-102.
- Liu, J., Liu, F.H., Kong, X.J., 2010. PFC Numerical Simulation of Particle Breakage of Rock-Fill Dam. 12th Biennial International Conference on Engineering, Construction, and Operations in Challenging Environments; and Fourth NASA/ARO/ASCE Workshop on Granular Materials in Lunar and Martian Exploration.
- Liu, S., Sun, Y., Shen, C., et al., 2020. Practical nonlinear constitutive model for rockfill materials with application to rockfill dam. *Comput. Geotech.* 119, 103383.
- Liu, H.L., Yang, G., 2009. FFC2D numerical analysis of model testing of earth and rock-fill dam on shaking table. *Journal of Disaster Prevention and Mitigation Engineering*. 5, 5–10 in Chinese.
- Liu, H., Zou, D., Liu, J., 2014a. Constitutive modeling of dense gravelly soils subjected to cyclic loading. *Int. J. Numer. Anal. Meth. Geomech.* 38 (14), 1503–1518.
- Liu, J., Zou, D., Kong, X., 2014b. A three-dimensional state-dependent model of soil-structure interface for monotonic and cyclic loadings. *Comput. Geotech.* 61, 166–177.
- Liu, J., Zou, D., Kong, X., 2018. Three-dimensional scaled memory model for gravelly soils subject to cyclic loading. *J. Eng. Mech.* 144 (3), 04018001.
- Luding, S., 2006. About contact force-laws for cohesive frictional materials in 2D and 3D. *Behavior of granular media* 9, 137–147.
- Luis, A., Ismael, I., Guillermo, N., 1985. Performance of cogoti dam under seismic loading// *Concrete Face Rockfill Dams-Design. Construction and Performance*, ASCE, New York.
- Ma, G., Chen, Y., Yao, F., et al., 2019. Evolution of particle size and shape towards a steady state: Insights from FDEM simulations of crushable granular materials. *Comput. Geotech.* 112, 147–158.
- Manso, J., Marcelino, J., Caldeira, L., 2018. Crushing and oedometer compression of rockfill using DEM. *Comput. Geotech.* 101, 11–22.
- Marigo, M., Stitt, E.H., 2015. Discrete element method (DEM) for industrial applications: comments on calibration and validation for the modelling of cylindrical pellets. *Kona Powder Part. J.* 32, 236–252.
- Nie, Z., Zhu, Y., Wang, X., et al., 2019. Investigating the effects of Fourier-based particle shape on the shear behaviors of rockfill material via DEM. *Granular Matter* 21 (2), 1–15.
- Ning, F., Liu, J., Kong, X., et al., 2020. Critical state and grading evolution of rockfill material under different triaxial compression tests. *Int. J. Geomech.* 20 (2), 04019154.
- Pastor, M., Zienkiewicz, O.C., Chan, A.H.C., 1990. Generalized plasticity and the modeling of soil behavior. *Int J Numer Anal Methods Geomech.* 14 (3), 151–190.
- Powrie, W., Harkness, R.M., Zhang, X., et al., 2002. Deformation and failure modes of drystone retaining walls. *Géotechnique*. 52 (6), 435–446.
- Qu, Y., Zou, D., Kong, X., et al., 2019. Seismic damage performance of the steel fiber reinforced face slab in the concrete-faced rockfill dam. *Soil Dyn. Earthquake Eng.* 119, 320–330.
- Qu, Y., Zou, D., Chen, K., et al., 2021. Three-dimensional refined analysis of seismic cracking and anti-seismic measures performance of concrete face slab in CFRDs. *Comput. Geotech.* 139, 104376.
- Saberi, M., Annan, C.D., Konrad, J.M., 2019. Implementation of a soil-structure interface constitutive model for application in geo-structures. *Soil Dyn. Earthquake Eng.* 116, 714–731.
- Saiang, D., 2010. Stability analysis of the blast-induced damage zone by continuum and coupled continuum-discontinuum methods. *Eng. Geol.* 116 (1), 1–11.
- Silvani, C., Bonelli, S., Philippe, P., et al., 2008. Buoyancy and local friction effects on rockfill settlements: A discrete modelling. *Comput. Math. Appl.* 55 (2), 208–217.
- Song, W., Huang, B., Shu, X., et al., 2019. Interaction between railroad ballast and sleeper: a DEM-FEM approach. *Int. J. Geomech.* 19 (5), 04019030.
- Tran, T.H., Venier, R., Cambou, B., 2009. Discrete modelling of rock-ageing in rockfill dams. *Comput. Geotech.* 36 (1–2), 264–275.
- Tu, F., Ling, D., Hu, C., et al., 2017. DEM-FEM analysis of soil failure process via the separate edge coupling method. *Int. J. Numer. Anal. Meth. Geomech.* 41 (9), 1157–1181.
- Wang, T., Sheng, Q., Xiong, J., 2007. Research on numerical simulation of natural caving method based on particle flow method. *Chin. J. Rock Mech. Eng.* S2, 4202–4207 (in Chinese).
- Wen, L., Li, Y., 2020. Seepage control effect of a concrete face rockfill dam on a deep overburden foundation. *IOP Conference Series: Earth and Environmental Science*. IOP Publishing. 531 (1), 012038.
- Xiao, Y., Liu, H., Zhang, W., et al., 2016. Testing and modeling of rockfill materials: A review. *J. Rock Mech. Geotech. Eng.* 8 (3), 415–422.
- Xu, B., Zhou, Y., Zhou, C., et al., 2018. Dynamic responses of concrete-faced rockfill dam due to different seismic motion input methods. *International Journal of Distributed Sensor Networks*. 14(10): 1550147718804687.
- Xu, B., Zou, D., Liu, H., 2012. Three-dimensional simulation of the construction process of the Zipingpu concrete face rockfill dam based on a generalized plasticity model. *Comput. Geotech.* 43, 143–154.
- Yu X, Wang Y, Wang G, et al., 2022. Study on Working Behaviors and Improvement Strategies of Concrete Cutoff Wall with Slurry Cake in Thick Soil Foundation. *International Journal of Geomechanics*, 2022, 22(6): 04022075.
- Yu, X., Wang, Y., Tulamaiti, Y., et al., 2021. Refined numerical simulation of a concrete cut-off wall in the thick overburden of dam foundation. *Structures* 2021 (33), 4407–4420.
- Zarfl, C., Lumsdon, A.E., Berlekamp, J., et al., 2015. A global boom in hydropower dam construction. *Aquat. Sci.* 77 (1), 161–170.
- Zhang, Z.T., Gao, W.H., Wang, X., et al., 2020. Degradation-induced evolution of particle roundness and its effect on the shear behaviour of railway ballast. *Transp. Geotech.* 24, 100388.
- Zhang, J.M., Yang, Z., Gao, X., et al., 2015. Geotechnical aspects and seismic damage of the 156-m-high Zipingpu concrete-faced rockfill dam following the Ms 8.0 Wenchuan earthquake. *Soil Dyn. Earthquake Eng.* 76, 145–156.
- Zhang, G., Zhang, J., 2008. Unified modeling of monotonic and cyclic behavior of interface between structure and gravelly soil. *Soils Found.* 48 (2), 231–245.
- Zhao X, Xu J, Zhang Y, et al., 2018. Coupled DEM and FDM algorithm for geotechnical analysis. *International Journal of Geomechanics*. 18(6): 04018040.
- Zhou, W., Ma, G., Liu, J.Y., et al., 2018. Review of macro- and mesoscopic analysis on rockfill materials in high dams. *SCIENTIA SINICA Technologica*. 48 (10), 1068–1080.
- Zhou, M., Song, E., 2016. A random virtual crack DEM model for creep behavior of rockfill based on the subcritical crack propagation theory. *Acta Geotech.* 11 (4), 827–847.
- Zhou, W., Wang, D., Ma, G., et al., 2020. Discrete element modeling of particle breakage considering different fragment replacement modes. *Powder Technol.* 360, 312–323.
- Zienkiewicz, O.C., Chan, A.H.C., Pastor, M., et al., 1998. Computational geomechanics with special reference to earthquake engineering. John Wiley & Sons, New York.
- Zou, D.G., Kong, X.J., 2003. GEOtechnical DYNAMIC Nonlinear Analysis GEODYNA User Manual. Institute of Earthquake Engineering, Dalian University of Technology, Dalian in Chinese.
- Zou, D.G., Xu, B., Kong, X.J., 2009. Study of effect of nail-toed panel on stability of high earth-rockfill dam slope. *Journal of Dalian University of Technology*. 49 (05), 675–679 in Chinese.
- Zou, D., Xu, B., Kong, X., et al., 2013. Numerical simulation of the seismic response of the Zipingpu concrete face rockfill dam during the Wenchuan earthquake based on a generalized plasticity model. *Comput. Geotech.* 49 (APR.), 111–122.

## Further reading

- Chen, S., He, Q., Cao, J., 2018b. Seepage simulation of high concrete-faced rockfill dams based on generalized equivalent continuum model. *Water Sci. Eng.* 11 (03), 78–85.